

# Toward an Adhesion Based Measurement of Strain-Dependent Surface Stress in Soft Solids

by  
Jeremy K. Thaller

Professor Katharine E. Jensen, Advisor



A thesis submitted in partial fulfillment  
of the requirements for the  
Degree of Bachelor of Arts with Honors  
in Physics

WILLIAMS COLLEGE  
Williamstown, Massachusetts  
May 18, 2019



# Abstract

Surface stress, or surface tension, is a fundamental material property of interfaces. However, our understanding of solid surface tension and how it changes with deformation remains limited because it is difficult to measure in traditional stiff materials. Soft materials, including gels, provide a unique opportunity to measure these fundamental properties because they can be stretched elastically to very large strains. In this thesis, we have developed a new, adhesion-based approach to measure the solid surface stress of compliant materials as a function of applied strain. We measure the spontaneous indentation depth as a function of radius for rigid spheres adhered to compliant, sticky substrates, then fit the results to theory to obtain the surface stress,  $\Upsilon$  and adhesion energy,  $W$ . By subsequently stretching the substrates biaxially and repeating the experiment, we obtain  $\Upsilon$  and  $W$  as a function of strain,  $\epsilon$ . This approach is applicable to a wide range of soft materials. In this thesis, we report preliminary measurements for two types of polydimethylsiloxane (PDMS).



# Executive Summary

This thesis describes a new method for measuring strain dependent surface stress in soft solids, as well as the corresponding measurements for two silicone polymer gels. Over the past several years, attempts to measure surface stress in gels have returned a cornucopia of conflicting results, differing significantly in similar materials. Recently, Xu, Jensen *et al.* (2017) suggested that this discrepancy is an artifact of the strain state of the gels, and made the first direct measurement of strain-dependent surface stress,  $\Upsilon(\epsilon)$ , in solids [1]. In this paper, the authors reported that the surface stress changed dramatically under applied strain. At 18% strain, the surface stress more than doubled. This dramatic change in surface stress was a surprising result and a topic of controversy in the field.

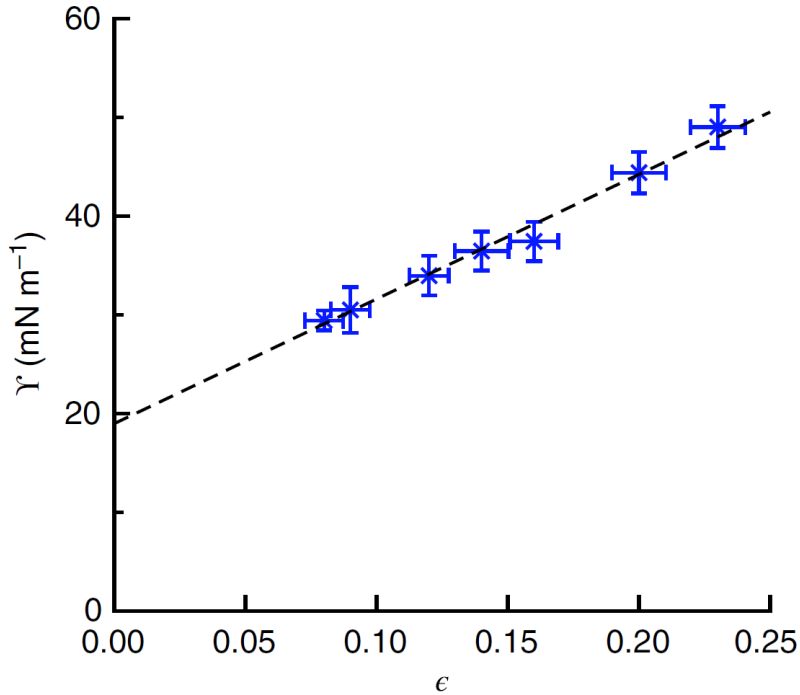


Figure 1: The first direct measurement of strain dependent surface stress in solids from Xu Jensen *et al.* (2017) [1]. Using a compliant silicone gel, surface stress,  $\Upsilon$ , was found to grow linearly as a function of strain,  $\epsilon$ .

Over the past year, we have developed a new method for measuring  $\Upsilon(\epsilon)$  as well as strain-dependent adhesion energy,  $W(\epsilon)$ , in soft solids. By measuring the spontaneous indentation depth of rigid spheres over a range of sizes, we can calculate  $\Upsilon$  and  $W$  using theory derived from our understanding of soft adhesion. Our adhesion-based technique can be applied to a wide variety of stretchable materials. Additionally, we have built our own equibiaxial stretching apparatus, improving upon the earlier published design [1] to produce nearly twice the strain in identical materials. Using this technique, we have measured the adhesion energy and surface stress in two types of silicone, as well as preliminary  $\Upsilon(\epsilon)$  measurements as we work towards recreating the surprising 2017 measurement.

Our  $\Upsilon$  and  $W$  measurements for PDMS silicone on glass (zero applied strain) are encouraging. Measurements of spontaneous indentation depth,  $d$  vs. the radius  $R$  return solid fits with minimal noise. Additionally, the calculated values values for  $\Upsilon$  and  $W$  agree with previous measurements.

### No Applied Strain (On Glass)

Gelest 9:1 ( $E=6.3\text{kPa}$ )

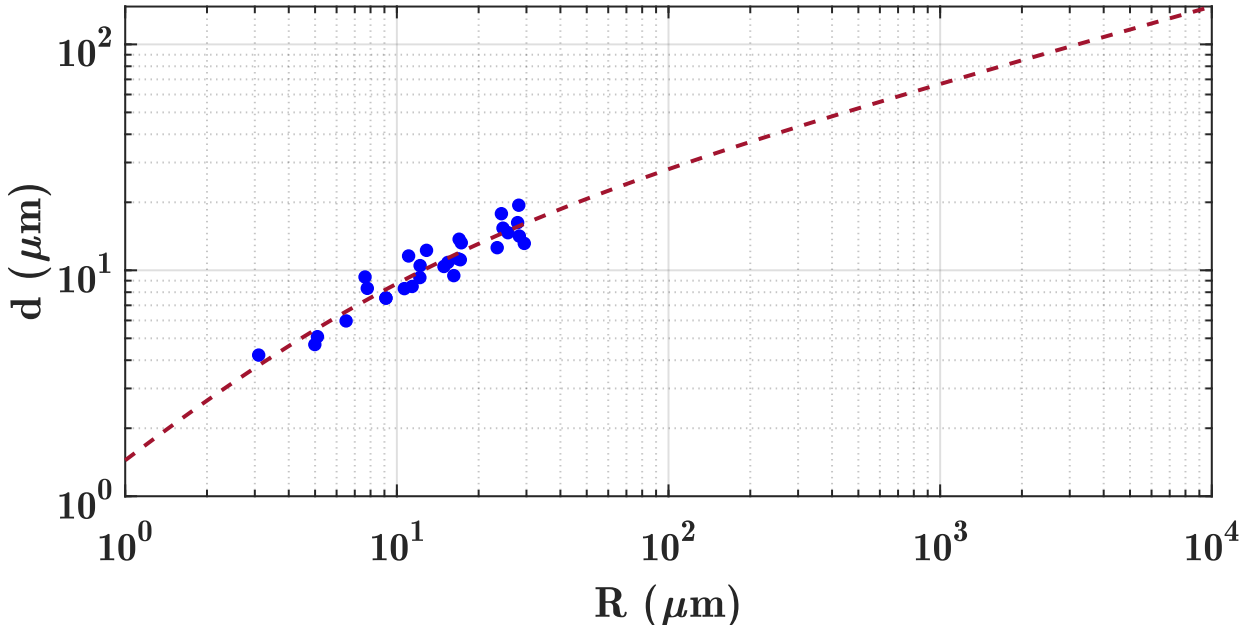


Figure 2: Plot of the spontaneous indentation depth,  $d$ , vs. radius,  $R$ , for many silica beads sinking into a soft silicone substrate. By considering the elastocapillary adhesive forces acting on the sphere, we fit an equation (Equation 2.9) to the  $d$  vs.  $R$  plot for a Gelest silicone sample (plotted here as the red dashed line). The best fit line returns parameters of  $W = 53 \text{ mNm}^{-1}$  and  $\Upsilon = 32 \text{ mNm}^{-1}$ .

Currently, the depth vs. radii measurements for PDMS on a stretchable substrate contain a significantly greater amount of noise than for the same substrate adhered to glass. Until the noise level is reduced, we cannot fit our data to extract  $\Upsilon$  and  $W$  values. However, our

preliminary results suggest that the surface stress in gels does significantly change under strain. Figure 4.6 demonstrates visually this  $\Delta\Upsilon$  for a single silica sphere sitting in a silicone substrate. As the underlying gel is stretched, the surface tension increases, reducing the depth into which the sphere sits.

### Same Silica Sphere: Stretched vs. Unstretched

Gelest 9:1 190301 (E=6.3 kPa)

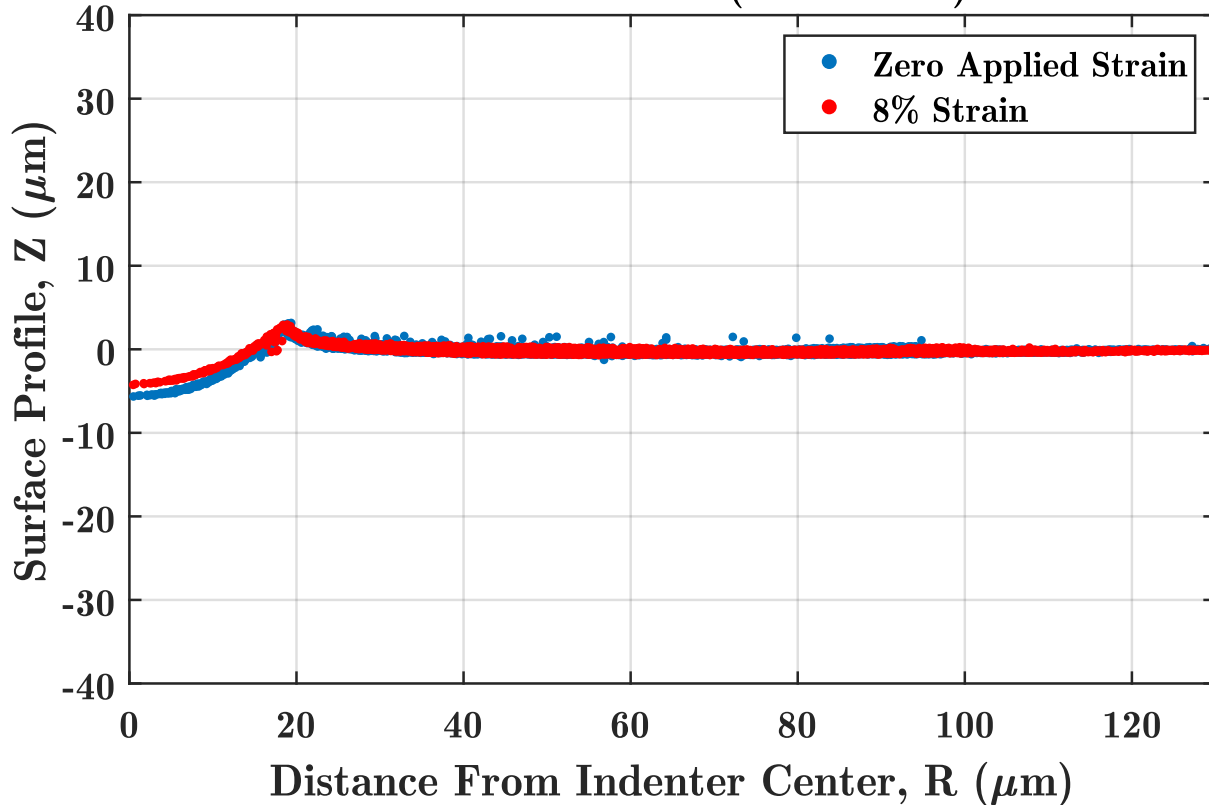


Figure 3: Side profile of the same silica sphere sitting in a silicone substrate before and after stretch. When a strain is applied, the sphere's indentation into the substrate is shallower. Substrate is Gelest PDMS with stiffness  $E = 6.3 \text{ kPa}$ .



# Acknowledgements

I would like to begin first and foremost by thanking my advisor, Professor Katharine Jensen. Looking back, Kate has had an incredibly positive impact on me and helped influence my life-trajectory after Williams more than anyone else. For that, I am eternally grateful. Undoubtedly, mein Freund and esteemed colleague Felix Knollmann has helped encourage me to produce my best (read: most aesthetic) work and refrain the procrastination that inevitably accompanies any long term project. Were it not for Katharine and Felix, I would never have even considered moving to Germany for graduate school.

Additionally, I would also like to thank my labmates, especially Josh Minwoo Kang, who taught me both how to cure silicone and analyze it. Also Abdullah Nasir. Furthermore, I really appreciate all the engineering help from Michael Taylor and Jason Mativi. Without them, most of my work would not have been possible.

I also would like to thank my friends that have made my time at Williams such an enjoyable experience. From forging a bird painting with Sarah Ritzmann (to trick Marshall Borrus) to buying 10 lbs of grits at Wild Oats with Lucas Estrada, I'm blessed to have filled my — albeit, scarce — free-time with such bizarre and memorable experiences. That lack of free time is in part a result of my career on the track team. I want to thank my coaches and teammates who have made these last four years such an incredible experience. Specifically, I want to thank coach Hoey and coach Barron, who may have taught me more about life than running itself.

Lastly, I would like to thank my parents. For raising me to always be curious, allowing me to attend Williams, and always supporting me in whatever ways they can, I am extremely grateful and fortunate.



# Contents

<b>Abstract</b>	i
<b>Executive Summary</b>	ii
<b>Acknowledgements</b>	v
<b>1 Introduction</b>	1
1.1 Motivations . . . . .	1
1.2 Historical Context . . . . .	1
1.2.1 Development of Surface Tension . . . . .	1
1.2.2 Surface Tension in Solids . . . . .	2
1.2.3 Surface Stress Effects in Soft Solids . . . . .	3
1.2.4 Direct Measurement of Solid Surface Stresses . . . . .	4
1.3 Outline of the Thesis . . . . .	6
<b>2 Experimental Approach: Setup, Data Acquisition, &amp; Analysis</b>	7
2.1 Measuring Surface Stress via Adhesion . . . . .	7
2.1.1 Beyond Hertzian Mechanics and JKR Theory . . . . .	7
2.1.2 Force Balance Derivation . . . . .	8
2.1.3 Experimental Approach . . . . .	10
2.2 Preparing a Substrate . . . . .	11
2.3 Stretching Apparatus . . . . .	12
2.3.1 Stretcher Design . . . . .	12
2.4 Calibration . . . . .	14
2.4.1 Measuring Strain . . . . .	14
2.5 Material Characterization . . . . .	16
2.5.1 Hertzian Contact Mechanics Derivation . . . . .	17
2.6 Putting it all Together . . . . .	19
<b>3 Data Acquisition and Image Analysis</b>	20
3.1 Fluorescent Confocal Microscopy . . . . .	20
3.2 Applying Fluorescent Confocal Microscopy to the Sample . . . . .	21
3.2.1 Raw Data Files . . . . .	23

<b>CONTENTS</b>	<b>vii</b>
3.3 Image Analysis . . . . .	25
3.3.1 Particle Location . . . . .	25
3.3.2 Depth and Radius Determination . . . . .	25
<b>4 Surface Stress and Adhesion Results</b>	<b>35</b>
4.1 Organosilicon Polymer Chemistry . . . . .	35
4.1.1 Silicone Preparation and Spin-Coating . . . . .	36
4.2 Preliminary Data: Gelest . . . . .	38
4.2.1 Standard Candles . . . . .	38
4.3 Dow-Corning PDMS . . . . .	43
4.4 Gelest and Dow-Corning PDMS Conclusions . . . . .	44
<b>5 Future Work</b>	<b>46</b>
5.1 Noise Minimization . . . . .	46
5.2 New Materials . . . . .	46
5.3 Future Techniques . . . . .	47
<b>A Stretching Apparatus Design</b>	<b>48</b>
A.1 Details of Stretcher Design . . . . .	48
<b>B Fluorescent Bead Recipe</b>	<b>51</b>
B.1 Preparation of a Fluorescent Bead Solution . . . . .	51
<b>C MATLAB Code</b>	<b>52</b>
C.0.1 Confocal Analysis Codes . . . . .	52
C.0.2 Strain Calculation Codes . . . . .	53
C.0.3 Silicone Characterization Measurements . . . . .	53

# List of Figures

1	Surface Stress vs. Strain in Silicone . . . . .	ii
2	Gelest W-Y Fit . . . . .	iii
3	Side Collapse Comparison . . . . .	iv
1.1	Surface Free Energy . . . . .	2
1.2	Three-Phase Diagram . . . . .	3
1.3	Three-Phase Diagram: Zoomed . . . . .	4
2.1	Spherical Cap Geometry . . . . .	9
2.2	Prepared Substrate Profile . . . . .	12
2.3	Side Profile of Stretching Apparatus . . . . .	13
2.4	Stretching Apparatus Design . . . . .	13
2.5	Bright-field stretch calibration images . . . . .	15
2.6	Particle-Locating for Stretch Calibration . . . . .	16
2.7	Bulk Modulus Test . . . . .	18
2.8	Bulk stiffness Fit . . . . .	18
3.1	Minsky Patent Diagram . . . . .	20
3.2	Fluorescent Confocal Microscopy . . . . .	21
3.3	Nikon Ti2 Microscope Base . . . . .	22
3.4	Confocal Setup . . . . .	22
3.5	The surface plane of a silica bead in silicone . . . . .	23
3.6	Particle Located: Normalized-Axes . . . . .	25
3.7	Particle Located: Stretched-Axes . . . . .	26
3.8	Particle Located: Top View . . . . .	27
3.9	Collapsed Side Profile . . . . .	28
3.10	Collapsed Side Profile: Zoomed . . . . .	29
3.11	Circle Fit . . . . .	30
3.12	Circle Fit Zoomed . . . . .	31
3.13	Small Sphere Side Profile . . . . .	32
3.14	Small Sphere Circle Fit . . . . .	33
3.15	Depth vs. Radius Example . . . . .	34

*LIST OF FIGURES*

ix

4.1	DMS-V31 . . . . .	35
4.2	HMS-301 . . . . .	36
4.3	Side Profile Comparison: 8% . . . . .	39
4.4	Side Profile Comparison: 22% . . . . .	40
4.5	Glass vs. Stretched d vs. R . . . . .	41
4.6	Gelest W-Y Fit . . . . .	42
4.7	D vs. R Dow-Corning . . . . .	43
4.8	Dow Corning W-Y Fit . . . . .	44
4.9	Side Collapse Tilt . . . . .	45
A.1	Stretching Apparatus Design Document . . . . .	49
A.2	Stretcher outer-ring . . . . .	50

# Chapter 1

## Introduction

### 1.1 Motivations

Soft condensed matter physics includes the study of colloids, liquid crystals, polymers, complex fluids, rubbers, foams, many biological materials, and — what we devote most of our time to studying in the Jensen lab — gels. From cosmetics to sticky notes, soft solids are ubiquitous in everyday life and are of growing interest due to their unique properties compared to traditional (hard) engineering materials. It is important to understand how such ubiquitous materials behave, especially when put under the strains of life. Accordingly, the topic of adhesion and wetting has been studied for hundreds of years, and yet, is a discipline with many mysteries still to be explored [2].

### 1.2 Historical Context

#### 1.2.1 Development of Surface Tension

Though few people may know the term, surface stress is a familiar concept in everyday phenomena: water droplets bead up into spheres, paperclips can float on water despite being made of dense iron, and water striders navigate the water's surface thanks to their hydrophobic legs. Each of these marvels is a result of **surface stress**,  $\gamma$ , the energetic cost per unit area to create new surface [3]. The water strider, for example, exerts a force on the water due to gravity. Because creating new surface costs energy, the water resists deformation, providing a restorative force that effectively balances the insect's weight to keep it afloat. Likewise, water droplets bead up and liquid surfaces are smooth because  $\gamma$  acts to minimize the surface-to-volume ratio of the liquid [4, 2].

Let's dissect the example of a water strider (rather than the water strider itself!). Water exists in the liquid phase when the thermal agitations are stronger than the cohesive attraction between the molecules, but not so strong that the water vaporizes. This dense yet disordered state consists of both molecules at the surface and molecules in the bulk. Any

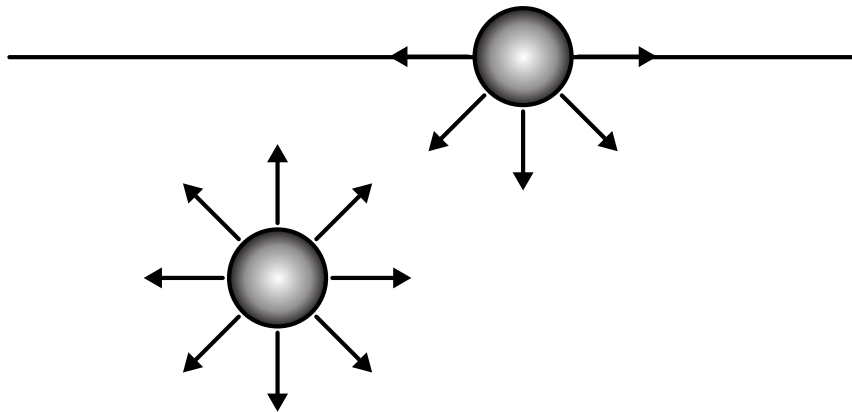


Figure 1.1: The cohesive forces acting on two molecules, one in the liquid’s bulk and the other at the liquid-gas interface. A molecule in the bulk has twice as many neighboring molecules than one on the surface, and thus, twice as many neighboring attractions.

given molecule in the bulk is surrounded equally by particles on all sides, resulting in symmetrically balanced forces in all directions. A surface molecule, however, is missing half of these attractions. Thus, the cohesive energy per molecule at the surface is roughly half that of a molecule in the bulk [2]. The difference in energy per unit area between particles in the bulk compared to the surface is known as the **surface free energy**,  $\gamma$ , often written as just surface energy. Equivalently,  $\gamma$  can also be defined as the reversible work per unit area to create new surface by cutting. This exposes new particles to the surface. When the surface of a fluid is “stretched,” however, new atoms or molecules arrive at the surface, maintaining the number of atoms per unit area as a constant value. Therefore, the surface energy is the same as the surface stress for a fluid and equal to a constant value. Because of this,  $\gamma$  and  $\Upsilon$  have are often referred to interchangeably as **surface tension**. While conceptually the energetics are similar in liquid materials, the situation becomes more complicated for materials which cannot flow.

### 1.2.2 Surface Tension in Solids

In metals, the origin of surface stress, on the atomic scale, derives from the crystalline structure. The epitaxial layer, or surface atoms, reside in a lower electron density and therefore a different equilibrium spacing than the bulk. The bulk atoms force the surface atoms to fit into the epitaxial overlayer of the crystalline substrate. As a result, the surface atoms are strained by the bulk, leaving the surface stressed by the underlying lattice [3].

Theoretical calculations for surface stress generally involve taking the derivative of the predicted surface free energy with respect to strain. Various methods for metals involve calculating the electronic density, the kinetic energy, and the electrostatic exchange-correlation<sup>1</sup>

---

<sup>1</sup>Forgoing the independent electron approximation, the electronic exchange is a measure of deflection due

[5]. Experimental measurements of surface stress have been around as early as the 1960's, though measurements of strain-dependent surface stress in stiff materials have only been attempted much more recently and returned scant results [6, 7, 8, 9, 10]. Metals are an incredibly useful building tool due to their strength<sup>2</sup>, but their stiffness<sup>3</sup> also makes measuring properties as a function of strain severely limited, as most metals will fracture after a few percent strain. For most solids, these surface effects go unnoticed in everyday life due to the overpowering effects of the bulk's elasticity compared to any surface energies [11, 12, 13, 14, 15, 16].

### 1.2.3 Surface Stress Effects in Soft Solids

For solids of small enough size or soft enough composition, the surface energies can compete with or even dominate the effects of the bulk, resulting in strange and counterintuitive material properties. For example, the addition of finite, microscopic, liquid droplets in a soft solid actually stiffens the material [17]. While removing solid material affects the elastic stiffness, it also increases the surface area. At length scales where surface effects dominate, this increase in surface area has a greater energetic cost, and thus leads to a stiffer solid. Further, surface stresses can drive liquid-like instabilities in soft solids, including rounding out sharp corners [18] and a solid-cylinder version of the Plateau-Rayleigh instability [19].

Early observations of the effect of  $\Upsilon$  in soft solids came from considering the wetting behavior of liquid droplets on soft solid surfaces [1, 20, 21, 22]. The traditional Young-Dupré picture of wetting is shown in Figure 1.2. This is clearly an unbalanced force diagram

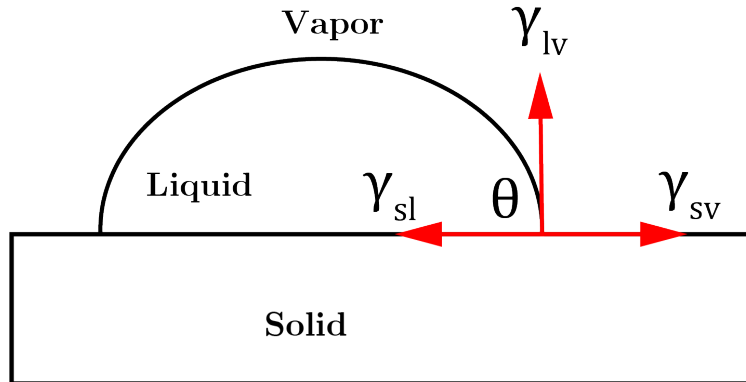


Figure 1.2: Classical Three-Phase Diagram of a liquid droplet on a solid substrate.

in vertical direction; the only vertical force component drawn is the liquid-vapor surface tension,  $\gamma_{lv}$ . The normal force from  $\gamma_{lv}$  must be balanced by the elastic substrate's resistance to deformation. Calculating this value, however, is still an open question. According to

to the presence of other electrons

<sup>2</sup>Strength: the maximum force per unit area a material can withstand

<sup>3</sup>Stiffness: the material's resistance to deformation via strain

continuum elastic theory, the stress exerted by  $\gamma_{lv}$  on the solid diverges at the contact line [20]. While the field of contact mechanics dates back to the 18th century, seemingly simple problems like a liquid droplet on an elastic surface are still not yet well understood and provide challenging questions when examined on a small enough scale.

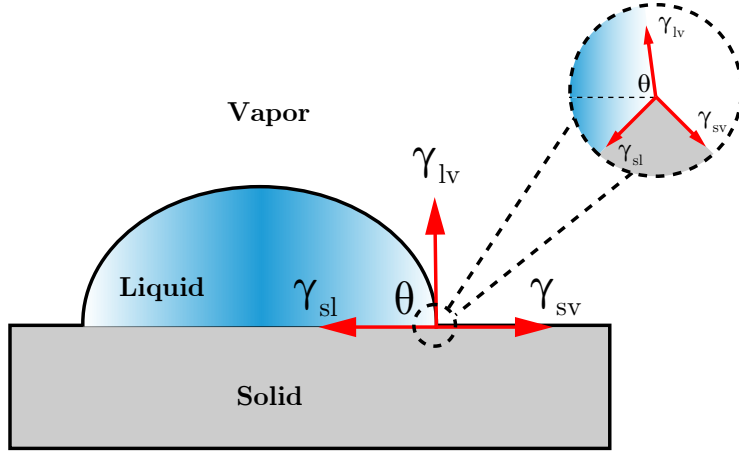


Figure 1.3: When inspected on the microscopic scale, the unbalanced three-phase diagram of Figure 1.2 is resolved by the deformation of the substrate. The liquid droplet indents into the solid and pulls the solid up slightly to wrap around itself.

Jerison *et al.* 2011 [20] found that modeling the deformation of the elastic substrate due to a liquid droplet fit best by incorporating both the finite thickness and surface tension of the substrate. This new model solved many issues with the previous best solution by Boussinesq: taking into account the finite thickness ensured that the deformations would go to zero far from the contact line, and the substrate's surface tension resolves the single stress singularity, eliminating the divergence of strain and vertical displacement at the contact point [23]. This gave us the first method to measure  $\Upsilon$  of a solid directly, tackling a long-standing problem in materials science.

#### 1.2.4 Direct Measurement of Solid Surface Stresses

The method of measuring the deformation of a soft, elastic solid imposed by the liquid droplet in Figure 1.2 was introduced by Jerison in 2011 [20] and later utilized by Style *et al.* in 2013 [21]. They measured the three-phase contact line geometry in Figure 1.3 without requiring any prior knowledge about the bulk elastic properties of the substrate material.

While this technique is effective, it is limited in its applications due to material properties. The method only works for immiscible fluids such that the gel does not absorb the surface droplets. Furthermore, the fluid must also have a low volatility; otherwise, the droplet would begin to evaporate while waiting for the surface deformations to settle. Since then, other methods have been developed, including an adhesion-based technique developed by Style

*et al.* in 2013 [24]. In soft adhesion, the deformation of a soft substrate due to contact with a rigid object depends partially on the surface stress, which can then be extracted using theory (derived in Chapter 2) [25, 26, 27]. Though the measurement is less direct, this adhesion based method does not suffer from the same material limitations and gives us another approach to measure  $\Upsilon$  [28, 29, 30, 31, 32, 33].

### Puzzling Surface Stress Measurements in Gels

Surface stress in soft solids is a topic of growing interest. Gels, for example, while classified as solid, are comprised mainly of fluid (by weight) and exhibit many properties that are more closely associated with liquids. Their rigidity is a result of a three-dimensional network of crosslinked polymers which entrap large amounts of liquid throughout<sup>4</sup> via capillary forces. The result is a solid whose stiffness is determined by the composition and temperature. Unlike in metals, elastocapillary physics plays a crucial role in determining a soft material's behavioral properties. Furthermore, because the surface stress in liquids is constant and equal to the surface energy of the substance ( $\Upsilon = \gamma$ ), it was largely assumed that deforming a gel would not have a significant effect on the surface tension, given that the fluid could flow back to the stretched surface of the gel.

Measurements of surface stress in soft solids (Table 1.1) in the past several years have yielded wildly varying results. It began to become clear that the surface stress of soft solids was not simply that of the fluid phase. The mystery of the discrepant  $\Upsilon$  measurements could

Silicone	Young's Modulus (kPa)	Measured $\Upsilon$ (mN m <sup>-1</sup> )	Reference
Sylgard 184	770	19	[28]
Gelest	5.6	20	[29]
Sylgard 184	2400	26	[30]
Dow Corning CY52-276A/B	3	30	[21]
Sylgard 184	18	30-70	[31]
Sylgard 184	1000	40-50	[32]
Dow Corning CY52-276A/B	3	42-59	[33]

Table 1.1: A Collection of Previously Measured  $\Upsilon$  Values

be solved if  $\Upsilon$  were not constant, but, instead, dependent on the deformation state of the material. The idea that  $\Upsilon$  may be strain dependent ( $\Upsilon(\epsilon)$ ) goes back to the classical theory of  $\Upsilon$  in metals, but had never been fully experimentally verified.

---

<sup>4</sup>For a more in depth explanation, see section 4.1

### Strain Dependence of Surface Stress in Traditional Solids

In contrast to a liquid, when the surface of a solid is stretched elastically, the number of atoms per unit area changes, such that generally  $\gamma \neq \Upsilon$  in solids [3]. The relationship between surface energy and surface stress can be derived through the use of the elastic deformation tensor  $\epsilon_{ij}$ , where  $i, j = 1, 2$ . We can then define  $d\epsilon_{ij}$  to be an infinitesimal and elastic (reversible) strain as a result of a variation in the surface area,  $A$ . The surface stress tensor,  $\Upsilon_{ij}$ , is the work associated with the variation in the excess free energy of the surface due to strain,  $\gamma A$ . Thus, we can write,

$$d(\gamma A) = A\Upsilon_{ij}d\epsilon_{ij}$$

Expanding out the first term,  $d(\gamma A) = \gamma dA + Ad\gamma$ . Utilizing symmetries, we can say that  $dA = A\delta_{ij}d\epsilon_{ij}$ , where  $\delta_{ij}$  is the Kronecker delta. Making the substitution, we find

$$\gamma dA + Ad\gamma = \gamma A\delta_{ij}d\epsilon_{ij} + Ad\gamma = A\Upsilon_{ij}d\epsilon_{ij}$$

And thus,

$$\Upsilon_{ij} = \delta_{ij}\gamma + \frac{\partial\gamma}{\partial\epsilon_{ij}} \quad (1.1)$$

This (1.1) is known as the Shuttleworth Equation, and clearly shows that both  $\gamma$  and  $\Upsilon$  in solids should be dependent on the strain state of the material.

Soft solids provide a unique opportunity to measure strain-dependent surface stress. Despite being a solid, soft solids, such as gels, can easily be stretched elastically. In 2017 Xu, Jensen et. al [1] made the first direct measurement of strain-dependent surface stress in solids. Their measurements suggest a surprisingly strong linear relationship between surface-stress and strain, measuring that the surface stress of their PDMS substrate more than doubled at 20% strain. However, their method of measurement is limited to a select combination of materials.

We have developed a method for measuring strain-dependent surface stress that is applicable to a wide variety of soft, compliant materials. We have measured  $\Upsilon$  and  $W$  in two varieties of PDMS using this soft adhesion approach. However, our attempts to measure these values as a function of strain have been met with an unexpected amount of noise. In this thesis, I present the full background, methods, and underlying physics of the process, as well as the  $\Upsilon$  and  $W$  measurements and preliminary  $\Upsilon(\epsilon)$  and  $W(\epsilon)$  work.

## 1.3 Outline of the Thesis

Building off the historical context described in this chapter, this thesis begins with a derivation of the modern theory of contact mechanics for soft solids. With this in mind, we proceed to outline the experimental design and setup in chapter 2, followed with an example of data acquisition and image analysis in chapter 3. Chapter 4 contains our preliminary surface stress and adhesion results for various materials. Finally, chapter 5 looks ahead, discussing possibilities for future experiments and improvements to the experimental process.

# Chapter 2

## Experimental Approach: Setup, Data Acquisition, & Analysis

In this chapter we discuss the setup of the experiment from start to finish. First we discuss the underlying theory required for the technique. Next, we walk through the experimental setup, followed by the process of acquiring and processing data for a single sphere. Finally we address the stretching apparatus, including its calibration process, and analyzing the results. Further details can be found in the appendices.

### 2.1 Measuring Surface Stress via Adhesion

#### 2.1.1 Beyond Hertzian Mechanics and JKR Theory

Hertzian mechanics, developed by Heinrich Hertz in the 1800's, allows for the calculation of stress and deformation based on the elastic moduli of the contacted surfaces, as well as their radii of curvature and applied force. These classical results are still relevant for isotropic materials in situations with minimal friction and small contact areas [34]. While Hertzian mechanics stood for a long time, it neglected to take into account the adhesion energy of the system.

In 1971, Johnson, Kendall, and Roberts (JKR) sought to remedy this omission by developing a classical theory of contact mechanics that balances the forces of adhesion with elasticity from the bulk and the surface free energy [35]. Today, it is still the standard theory used to interpret soft contact situations. However, it has recently been shown that while JKR theory is a great improvement over Hertzian mechanics, it breaks down in the elastocapillary regime [24]. Specifically, at lengths where

$$L \leq L_c = \frac{\Upsilon}{E} \quad (2.1)$$

the surface energies compete with those of the bulk and can no longer be ignored. Fittingly,  $L_c$  is referred to as the elastocapillary length. By understanding the role of surface tension

in soft adhesion, we can measure the physical properties of a balanced system in the elasto-capillary regime and hence measure the surface stress and adhesion energy from the balance of forces.

### 2.1.2 Force Balance Derivation

When materials are soft or small enough, three main forces balance to determine the contact mechanics of the system. Consider a marble sinking into a soft, sticky substrate. Adhesive forces increase the contact area between the marble and the substrate. Increasing the contact area has the effect of “pulling” the marble into the gel. As a consequence, the substrate is being compressed [vertically], which is counteracted by the elastic forces within the bulk. This compression also has the effect of stretching the surface of the substrate, which is counteracted by substrate’s surface tension. Below, we calculate the energy term associated with each of the forces acting on a dense sphere sinking into a soft substrate. Note, for such a small sphere, the force of gravity is negligible and need not be taken into consideration. For example, a silica (silicon-dioxide) microsphere has a density is 2.65 g/cm<sup>3</sup>. For a very large sphere with radius 50 microns, gravity only applies a force of roughly  $1.02 \times 10^{-8}$  N.

#### Elastic Energy

The energy required to make a circular indentation of radius  $R$  and depth  $d$  can be derived from Hertzian contact mechanics [36, 24, 37]. Contact between a sphere and an elastic half space<sup>1</sup> is a classic Hertzian contact problem. It is easiest to calculate the force and then integrate to determine the potential energy. For two elastic surfaces in contact with no externally applied forces, the force from elastic contact is:

$$F = \frac{4}{3} E^* R^{1/2} d^{3/2} \quad (2.2)$$

where

$$\frac{1}{E^*} = \frac{1 - \nu_{sphere}^2}{E_{sphere}} + \frac{1 - \nu_{substrate}^2}{E_{substrate}}$$

For a glass sphere sinking into a soft substrate,  $E_{sphere} \gg 1 - \nu_{sphere}^2$ , so this first term can be dropped as a reasonable approximation<sup>2</sup>. Thus we can approximate  $E^* \approx \frac{E_{substrate}}{1 - \nu_{substrate}^2}$ . Substituting this into equation (2.2), we find:

$$F \approx \frac{4}{3} \frac{E R^{1/2} d^{3/2}}{1 - \nu^2} \quad (2.3)$$

---

<sup>1</sup>i.e. the contact area is  $\ll$  the characteristic radius of the object. A flat plane can be thought of as  $R = \infty$

<sup>2</sup> $\nu_{SiO_2} \approx .17$  and  $E_{SiO_2} \approx 70 \times 10^9$  Pa

Because  $F = \frac{\partial U}{\partial d}$ , we can simply integrate equation (2.3) to obtain the energy relation:

$$U_{elastic} \approx \frac{ER^{1/2}d^{5/2}}{1 - \nu^2} \quad (2.4)$$

### Adhesion Energy

The free energy change on creating an interface via adhesion is the adhesion energy per area,  $W$ , multiplied by the surface area in contact (as found above). Namely,

$$U_{adhesion} \approx -2\pi WRd \quad (2.5)$$

### Surface Energy

$\Upsilon$  is the surface stress, which is equal to the energetic cost per unit area required to create surface via cutting or stretching the material. For a flat substrate being stretched via the indentation of a sphere, the energetic cost is

$$U_{surface} = \pi\Upsilon_{sv}\Delta A \quad (2.6)$$

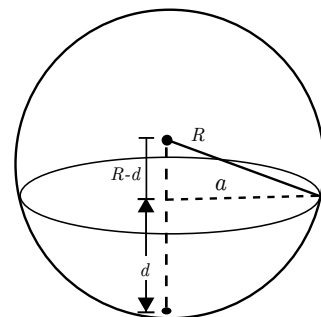
where  $\Delta A$  is the change in surface area when stretched by part of an indenting sphere (spherical cap). Determining the change in area is a simple geometrical problem.

$$\Delta A = A_{cap} - A_{circle}. \quad (2.7)$$

Let  $a$  be the base radius of the circle projected on the plane of the substrate's surface. Let  $R$  be the radius of the indenting sphere, and  $d$  be the depth into which it is stretching. We can find a relationship between these variables using the Pythagorean theorem.

Figure 2.1: Spherical Cap Geometry

$$\begin{aligned} a^2 + (R - d)^2 &= R^2 \\ a^2 + R^2 - 2Rd + d^2 &= R^2 \\ a^2 &= 2Rd - d^2 \\ a^2 + d^2 &= 2Rd \end{aligned}$$



Now, solving for  $\Delta A$  and using the above relationship in the last step, we find:

$$\begin{aligned}\Delta A &= 2\pi R d - \pi a^2 \\ &= \pi(a^2 + d^2) - \pi a^2 \\ &= \pi d^2\end{aligned}$$

Rewriting (2.6), we can simplify surface energy in this geometry as

$$U_{surface} = \pi \Upsilon_{sv} d^2 \quad (2.8)$$

### Force Balance

At static equilibrium, the sum of the energies is:

$$U_{total} = \Upsilon_{sv} \pi d^2 + \frac{c E R^{1/2} d^{5/2}}{1 - \nu^2} - 2\pi W R d$$

where  $c$  is a geometric factor to be determined in the next step. We can re-arrange the equation such that the sum of forces is equal to zero and differentiate both sides with respect to depth.

$$\begin{aligned}\frac{\partial U_{total}}{\partial d} &= \Sigma F = 0 \\ 2\pi \Upsilon_{sv} d + \frac{5c E R^{1/2} d^{3/2}}{2(1 - \nu^2)} - 2\pi W R &= 0\end{aligned} \quad (2.9)$$

Here,  $c = \frac{8}{5\sqrt{3}}$ . This value of  $c$  is chosen to recover classical JKR theory, which predicts an indentation of  $d = \left[ \frac{\sqrt{3}\pi W(1-\mu^2)}{2E} \right]^{2/3} R^{1/3}$  [24, 29, 35]. This energy balance was first published in 2013 by Style *et al.* in *Nature Communications* [24].

### 2.1.3 Experimental Approach

Equation 2.9 gives us a quantitative relationship between the spontaneous indentation depth,  $d$ , sphere radius,  $R$ , and key material properties:  $\Upsilon$ ,  $E$ ,  $\nu$ , and  $W$ . The Young Modulus,  $E$ , and the Poisson ratio,  $\nu$  of the substrate can be measured separately for the substrate material. The depth  $d$ , and the radius  $R$  of the sphere can be measured using fluorescent confocal microscopy, as described in Section 3.1. The only remaining terms,  $W$  and  $\Upsilon$ , the adhesion energy and the surface stress, respectively, can be determined with a two-parameter fit of  $d$  vs.  $R$ .

## 2.2 Preparing a Substrate

In the following section, we outline the process of preparing a soft substrate for testing. The process is similar for a zero-strain sample and a stretchable sample, and we make clear any distinctions between the two processes. Specific details for each substrate material tested can be found in Chapter 4.

Before preparing the substrate, we prepare the base surface on which the substrate will be coated. For a non-stretched sample, we use a glass coverslip, and for a stretched sample we use a thin, commercially available PDMS sheet from Specialty Manufacturing Incorporated. This base sheet is much stiffer ( $E \approx 1 \text{ MPa}$ ) than the substrate being tested. We first coat this base layer with fluorescent beads in order to later locate the bottom of our substrate. In preparing our substrate, there are two important factors to consider: thickness and evenness of the surface. The substrate must be thick enough such that the indenting spheres are not affected by the stiffness of the glass or PDMS base. This bottom layer of fluorescent beads allows us to easily gauge the thickness of our substrate. It is important that our substrate has an even surface, otherwise it is difficult to determine the sphere's depth,  $d$ . To achieve this, we use a technique called spin-coating where we place our uncured substrate (when it still is a liquid) on the base and spin it rapidly for a period of time. The angular momentum flings the fluid away from the center of the base. The result of this process is an even coating which will cure into our substrate over the next day.

Once cured, we deposit a second layer of fluorescent beads on the surface. These act as tracer particles which outline the indentation sphere. These fluorescent beads are on the order of  $10^3$  times smaller than the indentation sphere, and will thus, not influence how the sphere interacts with the substrate. Using fluorescent confocal microscopy, we are able to precisely locate each fluorescent bead and outline the indentation sphere. It is important that the bead spacing is dense enough to give a high resolution, yet not so dense as to become indistinguishable; high bead density presents a challenge for the MATLAB particle locating software. For a stretchable sample, we place the substrate, now cured onto the stretchable PDMS base, onto the lubricated stretching apparatus (described below). It is important to remove any small bubbles on the stretcher's ring to ensure an airtight seal.

The final preparation step is to sprinkle silica spheres of varying size on top of the silicone. This should be done at least 30 minutes before collecting data so that the spheres have time to settle into an equilibrium state into the silicone. From a side view, the final setup should look like Figure 2.2.

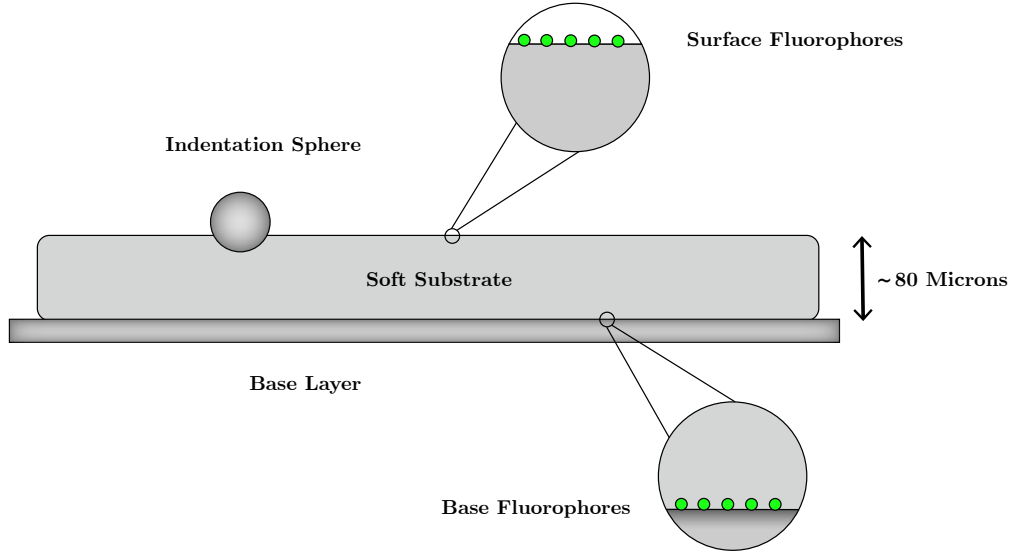


Figure 2.2: Side profile of a prepared substrate sample. There are two layers of fluorescent beads: the bottom layer is used to measure the substrate's thickness, and the surface layer is used to outline the profile of the larger, indenting sphere. The soft substrate sits on a base layer, namely glass or a stretchable PDMS silicone.

## 2.3 Stretching Apparatus

Our interest is not just in measuring  $W$  and  $\Upsilon$  for a given substrate, but in understanding how those values change when under strain. To accomplish this, we designed and built our own equibiaxial stretching apparatus capable of maintaining up to 35% strain in our silicone samples. The design is based off of previous work designed for stretching biological tissues [38] and is similar in design to the apparatus used in the 2017  $\Upsilon(\epsilon)$  measurements [1]. Below is a general description of the design; detailed design documents can be found in Appendix A.

### 2.3.1 Stretcher Design

Geometrically, the stretching apparatus is constructed of two concentric cylinders connected at the base to create a channel between them. The top of each ring is flat, apart from a slight chamfer to reduce the risk of ripping the sheet as it is stretched. Each ring is then coated in Dow-Corning vacuum grease to make a seal. It is critical that the inner ring has an ample amount of grease so that when a vacuum is pulled in the channel, the sheet will stretch from the center outwards and not from the edges inwards. The sheet is held in place with an o-ring wrapped around the outside of the cylinder, which is then clamped down by a removable outer ring using a tension clamp. The tension provided by the o-ring and clamp ensures that a solid vacuum is kept and the edges of the sheet are minimally stretched into the trough.

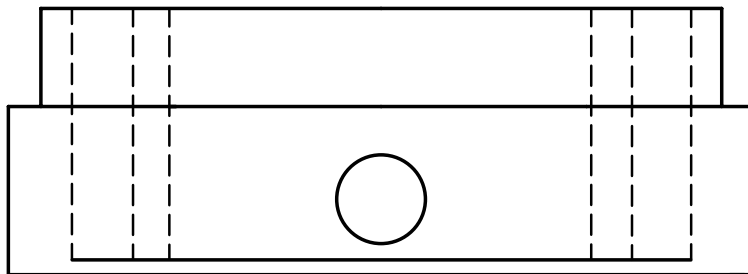


Figure 2.3: Side profile of the stretching apparatus. Note the channel attached at the base, and the large center hole at the base where the substrate can be accessed by the microscope.

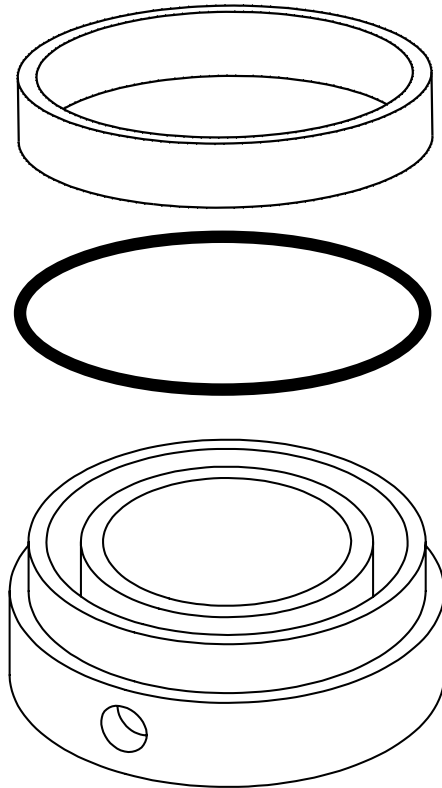


Figure 2.4: Exploded view of the stretching apparatus. The substrate goes on top of the base (substrate side down). It is then held down with an o-ring, which sits on the outside ledge. A second ring sits on top of the o-ring and is then held down by the microscope mount (not pictured).

A tapped screw hole on the side of the apparatus connects the chamber to a syringe via thin, plastic tubing. To pull a vacuum in the channel, we withdraw air using a syringe pump. This allows us to have a consistent withdraw rate and control the amount of air withdrawn to a high degree of precision. A deconstructed representation of the stretching apparatus can be found in Figure 2.4.

## 2.4 Calibration

Originally, we intended to calculate the strain induced by the vacuum by predicting the induced strain based on the amount of air withdrawn from the stretching apparatus. To measure strain, we withdraw air from the syringe and measure the movement of glass spheres adhered to the surface using a 10x air lens on our Nikon confocal microscope. Using the transmission detector allows us to image the surface of our material with a wide field of view. Strain percentage is calculated using MATLAB code [1].

There are several challenges in calibrating the induced strain. First, the stretching apparatus works best when a large strain is applied. Applying small strains one after another works, but there is a threshold to induce stretch. No stretching change is visible if less than 2 ml is withdrawn from the cylinder per increment. Thus, there is a limited resolution to our calibration data, which would not be a problem if the strain was linear. However, preliminary measurements indicated that the applied strain was nonlinear. This agrees with the previous results [38] obtained using a similar device. Lastly, the most significant challenge with calibrating strain is that we change substrates often. Even if we were to use the same exact sample, by removing it and setting up the device again, there is no way to standardize a zero-applied strain point. To prepare the stretching device, the sample is placed over the opening and a rubber o-ring is placed around the sample to help affix it in place. The sample must then be stretched and wiggled around slightly to remove any snags that could jeopardize the vacuum's efficacy. This means that every time a new sample is prepared, it is in an unknown and unique state of induced strain. Furthermore, before applying any strain, the substrate could be loose and uneven. Thus, to flatten the sample it must be stretched slightly.

It was thus determined best to measure strain using the confocal every time we applied a new strain to the silicone substrate and compare it to the substrate's original state. This also assured us that we knew the correct strain value to a higher precision for any given data set.

### 2.4.1 Measuring Strain

To determine the induced strain, we maximize the field of view and track the relative location of the indentation spheres. This allows us to see how more spheres are shifting, and thus gives a more accurate estimate of induced strain. As such, we decided to switch to the bright-field to image the spheres for each strain. We used a 10x air lens in conjunction with the transmission detector on our Nikon A1R Confocal. We adjust the settings to give decent contrast, but it is more important to have the spheres in focus. Each sphere reflects light, and it is this reflection that our particle locating software tracks after some image processing. An example image is located below (Fig.2.5), next to the same image after adjusting the contrast to help our tracking software with particle locating:

To track how the substrate stretches, we first find a centrally located group of spheres, or “constellation.” A good constellation is one that easily identifiable for relocation and

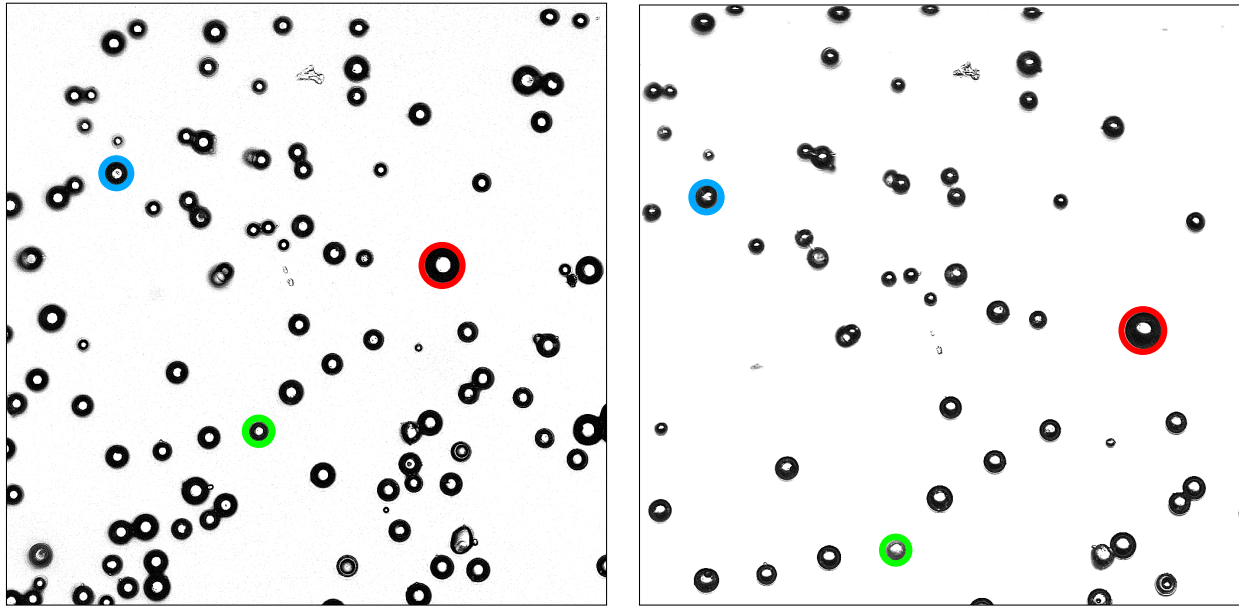


Fig. A

Fig. B

Figure 2.5: Fig. A shows the sample before stretching, and Fig. B shows the sample after a 35% equibiaxial strain. To calibrate the induced strain of our substrate, we switch to the brightfield to have a wider field of view for calibration. The three colored circles have been added to highlight the same spheres before and after stretching. Both of the images are 1.68 mm × 1.68 mm.

tracking purposes, and one that has many discrete points in the field of view - i.e. there are plenty of non-overlapping spheres. It is an added bonus to find 4 spheres perpendicularly located, such that they form the tips of cross. This allows for quick strain estimations using the microscope's built-in measuring tools. Though not necessarily, this is useful for a preliminary strain calculation to ensure the substrate is not preferentially stretching in one direction. Asymmetric stretching could indicate that the substrate is caught in the apparatus. Not only does this ruin the symmetry assumptions being made for our calculation, but it could lead to the substrate tearing if more strain is being applied than expected.

To evacuate the cylinder of air, we use the Harvard Apparatus<sup>TM</sup> Elite Pro Syringe Pump with a 50 mL Luerlock syringe. Before beginning any stretching, we withdraw a few ml of air to ensure the substrate is flat and not sagging. At this point we take a picture of the brightfield and call it the “zero applied strain” image. We compare all stretched data to this image in order to determine the induced strain. Using MATLAB software, we can locate each sphere (Figure 2.6) and track their change in location for different strains. From this we can calculate the induced strain, a tensor of rank two. However, because we are stretching the substrate equally in all directions (equibiaxially), we can just look at the magnitude of the tensor and treat the strain as a scalar [1, 22]. Because of the geometry of the stretching apparatus, along with the way the silicone cures and the local strains induced by adhesion,

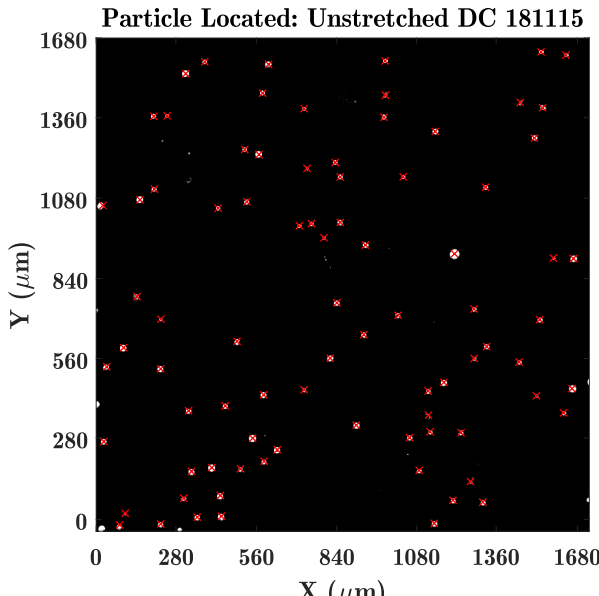


Fig. A

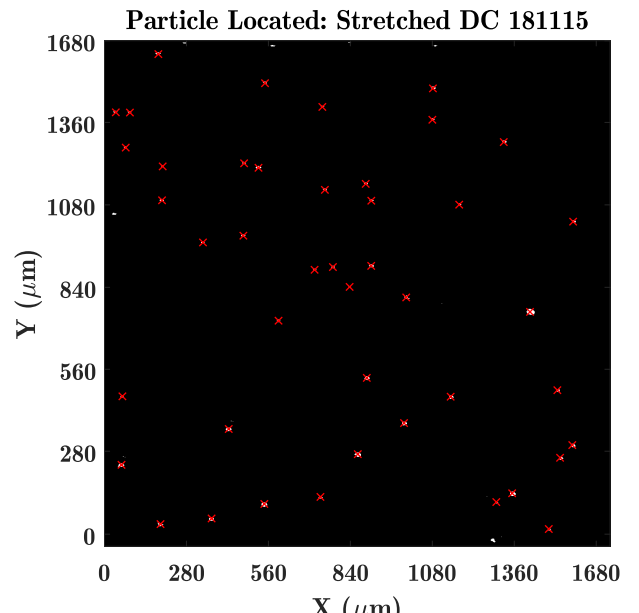


Fig. B

Figure 2.6: The spheres in Figure 2.5 as located by MATLAB software. By adjusting the contrast of the above images (Fig. 2.5), we remove all but the center highlighted reflection of each sphere. This allows our MATLAB software to consistently and reliably locate each sphere to track for strain calculation. The white circles are the center reflection of each sphere and the red crosses are the points being tracked for strain calibration by MATLAB.

we do not yet have a way to determine the true strain of the silicone. However, we are most interested in the slope of the  $\Upsilon$  vs.  $\epsilon$  curve,  $\Lambda$ , so this is not vitally important.

## 2.5 Material Characterization

To measure the stiffness of our substrate, we do not use the confocal measurement sample. Instead, when preparing the sample, we cure a surplus of the substrate material in a vial to test the bulk characteristics of the sample.

We take a standard bulk stiffness measurement using the Texture Technologies TA.XT Plus texture analyzer. A rigid cylinder with radius  $R = 1.5$  mm is slowly indented into the bulk substrate. The force response vs. indentation depth is recorded for several tests with varying starting heights and locations (See Figure 2.7). We use the average  $E$  value obtained from these tests in our  $W, \Upsilon$  fitting. The fitting process will be reviewed in Chapter 3.

### 2.5.1 Hertzian Contact Mechanics Derivation

We calculate the Young modulus for the bulk sample using classic Hertzian contact mechanics between a flat, rigid cylinder and an elastic half-space. Here,  $R$  is the radius of the indenter and  $d$  is the indentation depth of the probe. We can define the applied force as:

$$F = 2RE^*d \quad (2.10)$$

where

$$\frac{1}{E^*} = \frac{1 - \nu_1^2}{E_1} + \frac{1 - \nu_2^2}{E_2}$$

We are working with a large indenter and a geometry that fixes the contact area. For Silicone,  $\nu \approx .5$  for low strains; for the rigid cylinder,  $E \gg 1 - \nu^2$ , so we can ignore that term. From the force vs. depth information, we can write an equation for E:

$$\frac{1}{E^*} = \frac{2Rd}{F} \quad (2.11)$$

$$\frac{1 - \nu^2}{E} = \frac{2Rd}{F} \quad (2.12)$$

$$E = \frac{(1 - \nu^2) F}{2Rd} \quad (2.13)$$

$$E = \frac{(1 - .5^2) F}{2(1.5 \times 10^{-3})d} \quad (2.14)$$

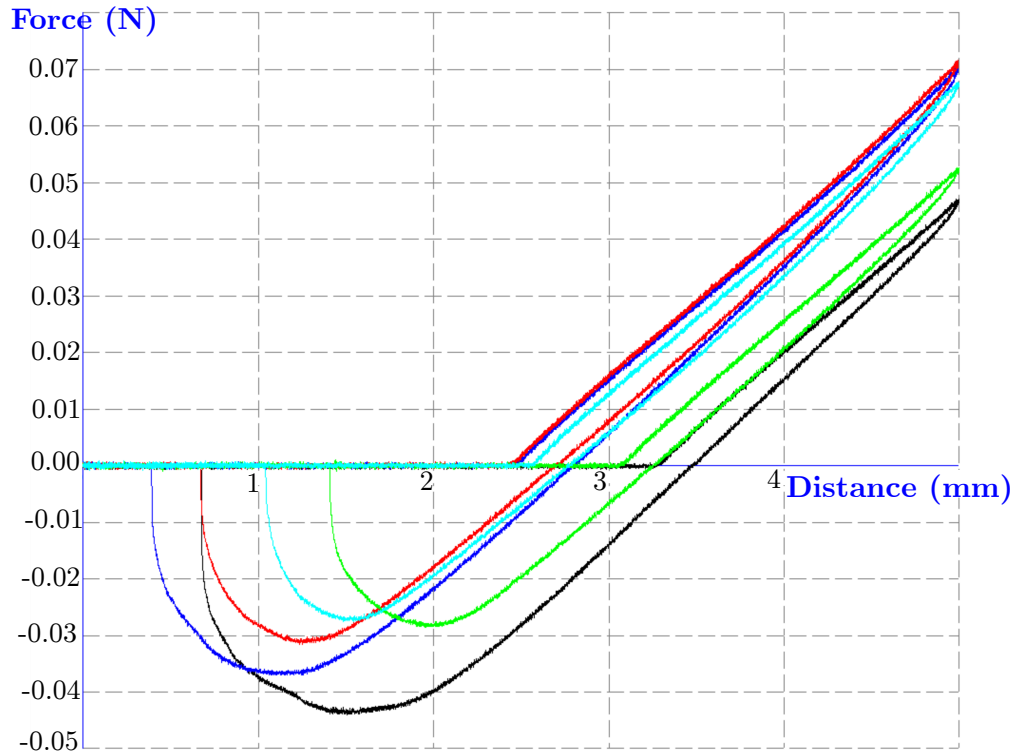


Figure 2.7: Force vs. indentation depth for a bulk sample of silicone. Each color represents a separate measurement at varying starting heights and locations on the sample.

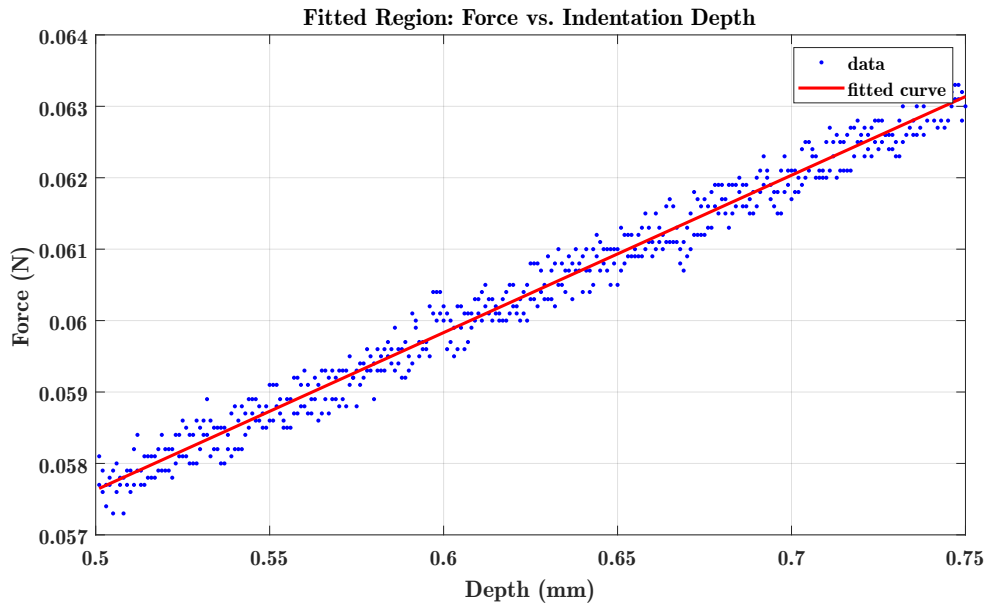


Figure 2.8: Fitting a line to the slope of the force vs. indentation depth for a bulk sample of the testing material allows us to use theory in order to calculate the stiffness,  $E$ .

## 2.6 Putting it all Together

Using the texture analyzer, we can measure  $E$  for our substrate. Next, we need a way to measure the spontaneous indentation depth,  $d$  vs. radius  $R$  for many spheres per sample. With these three values measured, only two terms in Equation 2.9 remain unknown,  $\Upsilon$  and  $W$ . To determine these unknown values, we can run a two parameter fit for Equation 2.9. Using our equibiaxial stretching apparatus, we can then repeat the  $d$  vs.  $R$  measurements for a range of strains to determine  $\Upsilon(\epsilon)$ . The process of collecting the  $d$  vs.  $R$  measurements for a single sphere is explained in Chapter 3.



# Chapter 3

## Data Acquisition and Image Analysis

### 3.1 Fluorescent Confocal Microscopy

Confocal microscopy is a technique capable of probing a sample with true three-dimensional optical resolution. The technique works by only allowing in focus light through a pinhole. By changing the plane of focus, one can traverse an object azimuthally and reconstruct a full three-dimensional image by compiling a “stack” of these images.

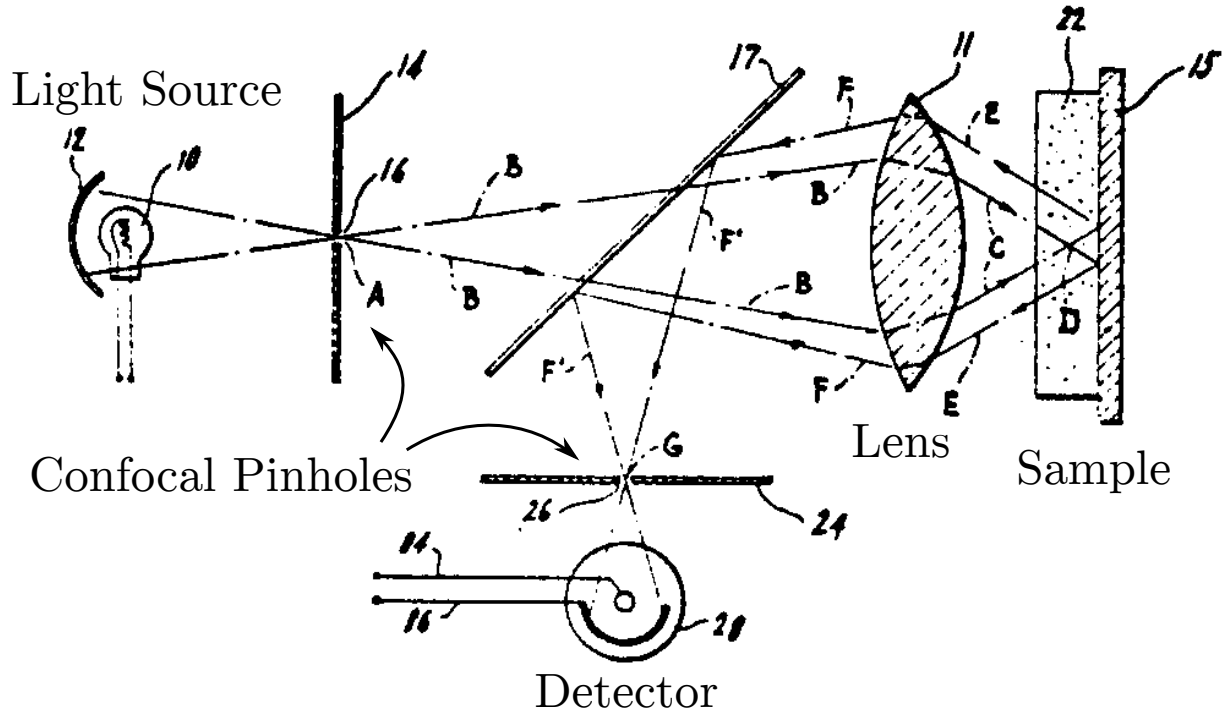


Figure 3.1: Diagram from Marvin Minsky's 1961 patent [39] for a confocal microscope. A pinhole before the photodetector blocks the out-of-plane light.

Fluorescent confocal microscopy works by the same general principle, only with the added complexity of optically-excitible fluorophores. These fluorophores absorb light from a narrow range of frequencies and re-emit fluorescent light at a different and narrow frequency which can then be measured. This allows for a greater resolution to larger objects, as well as the ability to detect surface features that would otherwise be invisible to the microscope.

Fluorescent confocal microscopy works by illuminating the specimen with a laser. The laser light passes through a pinhole, then is reflected by the dichroic mirror, and then focused by the objective lens on a small area of the specimen. The re-emitted light from the fluorophores (photoexcitation) has a longer wavelength than the laser light, so only it is transmitted through mirror. The photoexcitation light then passes through the pinhole where it travels to the photodetector. The net result of the process is a measurement of the photoexcitation light from a single plane of the probed sample. A diagram of this process can be found in Figure 3.2.

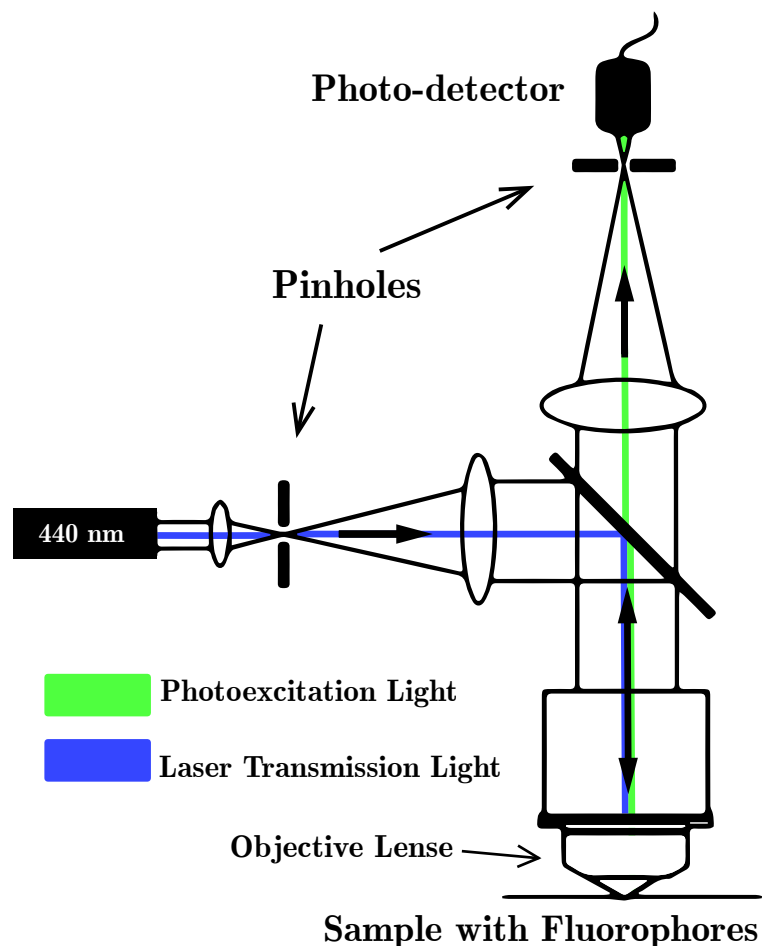


Figure 3.2: In fluorescent confocal microscopy, a dichroic mirror is used to filter the laser light from that emitted by the excited fluorophores.

## 3.2 Applying Fluorescent Confocal Microscopy to the Sample

In order to see our substrate with fluorescent confocal microscopy, we need to coat the surface of our substrate with tiny fluorescent beads (fluorophores). These have a diameter of about 40 nm. The detection of these fluorescent beads allows us to see the outline of the substrate's surface, as well as the indenting sphere, which displaces the beads beneath it as in sinks into the substrate. Directions for preparing a fluorescent bead solution in a borate buffer can be

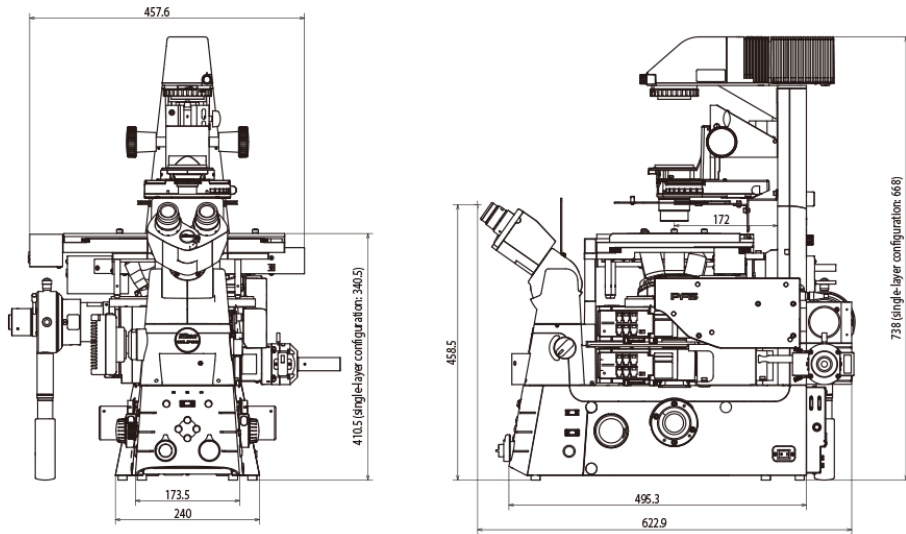


Figure 3.3: The Ti2 Eclipse Microscope Base. Image courtesy of Nikon [40].

found in Appendix Section B.1.

### Fluorescent Confocal Microscopy Data Collection

Data was obtained using the Nikon A1R HD25 Confocal Microscope with a Ti2 Eclipse used as the base. To take image stacks of the fluorescent beads, we use a 60x water-immersion objective lens with a numerical aperture of 1.2. We set the laser to 440 nm and adjust the power and gain (HV) as needed. Generally these values are around 5.0% and 40 volts, respectively. In order to get clear resolution for each bead, it is important not to saturate the photo-detector.

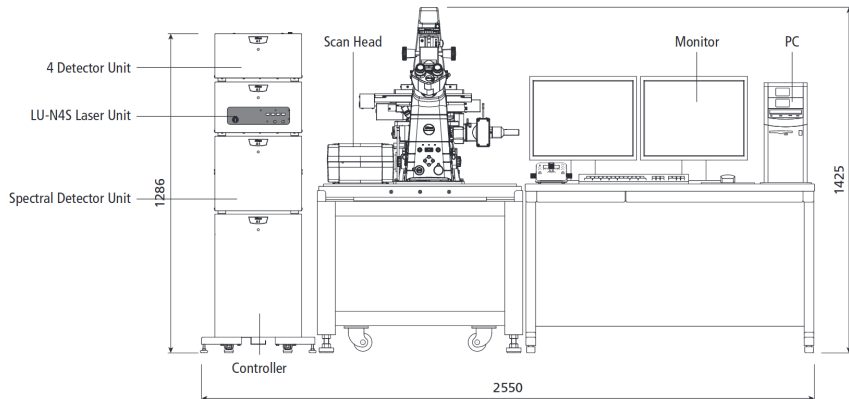


Figure 3.4: The general setup for the the confocal microscope. Image courtesy of Nikon [40].

For silica spheres ranging from  $5 - 50 \mu\text{m}$  in size, we have found the best scaling factor

(zoom) to be  $.104 \mu\text{m}/\text{pixel}$  in the horizontal plane for an image of  $1024 \times 1024$  resolution. We set the vertical step size (z-direction) to  $.225 \mu\text{m}/\text{px}$  or  $.25 \mu\text{m}/\text{px}$  depending on what the confocal recommended. Both provided adequate vertical resolutions. Using 16x averaging with the fast (resonant) scanner took up to 5 minutes per scan, but provided excellent resolution.

### 3.2.1 Raw Data Files

Using confocal microscopy, we collect a “stack” of images, detecting the light from the fluorescent beads. We have included an unprocessed data image (Figure 3.5) of the surface of a soft substrate with a glass bead adhered at upper left, displacing the surface out of this image plane.

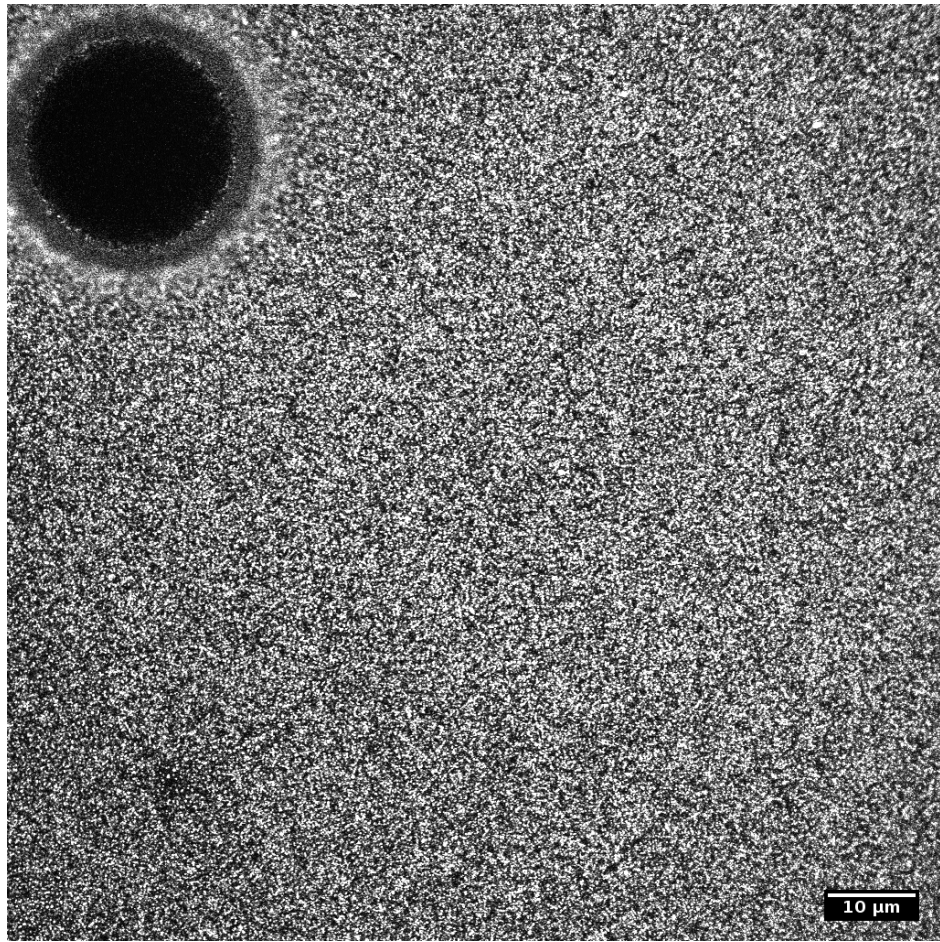


Figure 3.5: The surface plane of a silica bead in Gelest 9:1 silicone ( $E = 7.3 \text{ kPa}$ ). Radius of sphere =  $28.7 \mu\text{m}$ .

The object resembling a black hole in the top-left corner is the silica sphere. Each small white dot represents a fluorescent bead; together they create a sea of stars that outline

the surface plane and the silica sphere. Figure 3.5 is an example of the upper limit of bead coverage density. Any higher concentration of fluorescent beads could result in the photoexcitation light “bleeding” into the vertically adjacent photos in the stack. Note, the sphere is in the top corner of the image to provide maximum information about the leveling of the surface plane. We assume that the surface effects are symmetrical for zero applied strain and equibiaxial strain. Thus, it is more important to gather information in one direction to properly level the surface plane to determine the depth into which the sphere sinks.

For each sphere, we take a stack of 50–100 images, depending on the size of the sphere. Table 3.1 shows several vertical slices from the bottom of the sphere to just above the surface of the substrate.

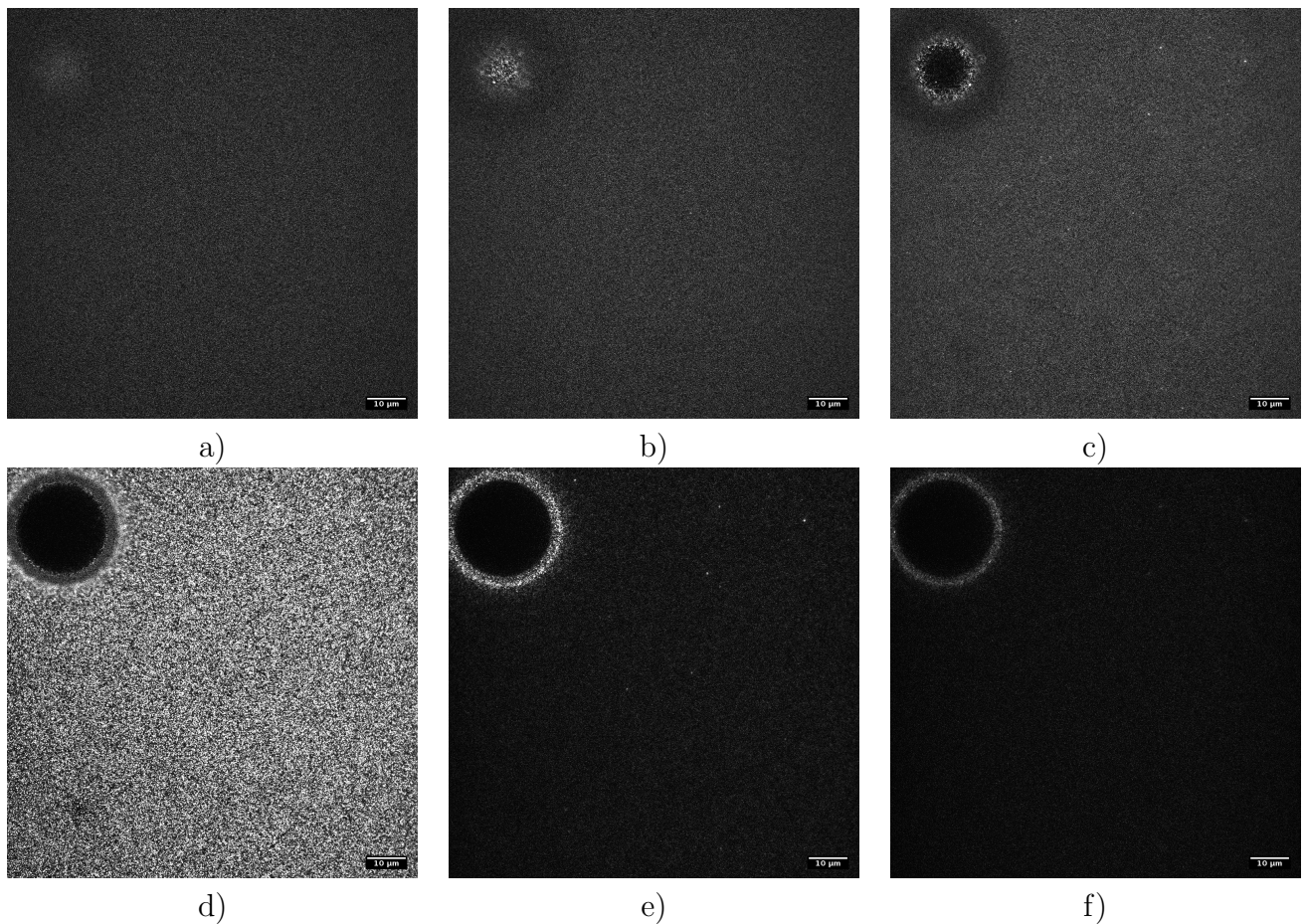


Table 3.1: Images a-f display the x-y plane of the same sample traversing vertically from below the silica sphere to above the surface plane. The scale bar in the bottom right corners represent 10  $\mu\text{m}$ .

## 3.3 Image Analysis

In the following section, we will step through the process of analyzing a single sphere. Recall that in order to determine the surface stress and adhesion energy, we must fit equation 2.9 to the depth vs. radius measurements for a collection of spheres.

### 3.3.1 Particle Location

We use a MATLAB program to locate the fluorescent beads in each 3D raw image stack. This is plotted in Figure 3.6 for the same adhered sphere as in Figures 3.5 and Table 3.1. The flat orange plane of points represents the substrate's surface, and the dark blue points are the fluorescent beads pushed underneath the microsphere as it sinks into the substrate. It is easy to see the outline of the microsphere, and we can use this information to determine its depth,  $d$  and radius  $R$  for the sphere. Figure 3.7 shows the same sphere but stretched in the vertical axis to showcase the fluorescent bead density towards the bottom of the sphere.

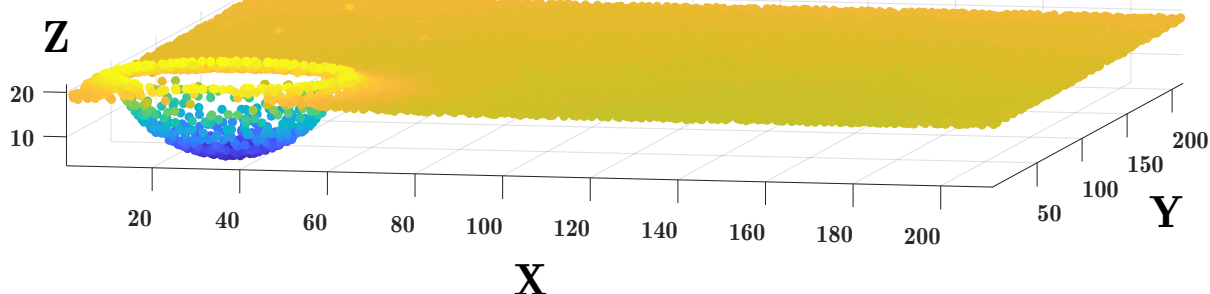


Figure 3.6: Using MATLAB software, we locate each of the fluorescent beads in a given image stack. Here, we've plotted the located beads for the same sphere as in Figure 3.5 and Table 3.1. The dense blanket of orange points represents the surface of the substrate, and the blue points are the fluorescent beads pushed beneath the silica sphere during indentation.

### 3.3.2 Depth and Radius Determination

After locating all the fluorescent beads and reconstructing our raw image in a useful format, we can then use this information to extract the depth and the radius of the sphere. To accomplish this, we first determine the center of the sphere as seen from the top (x-y plane) and collapse the surface profile azimuthally about the sphere's center position. Figure 3.9 depicts the x-z plane as a cross-section through center of the sphere. We only need half of the sphere's profile to fit a circle. This ensures we have a large field of view to properly level and determine the substrate's surface. Figure 3.10 provides a zoomed-in view of Fig. 3.9 to

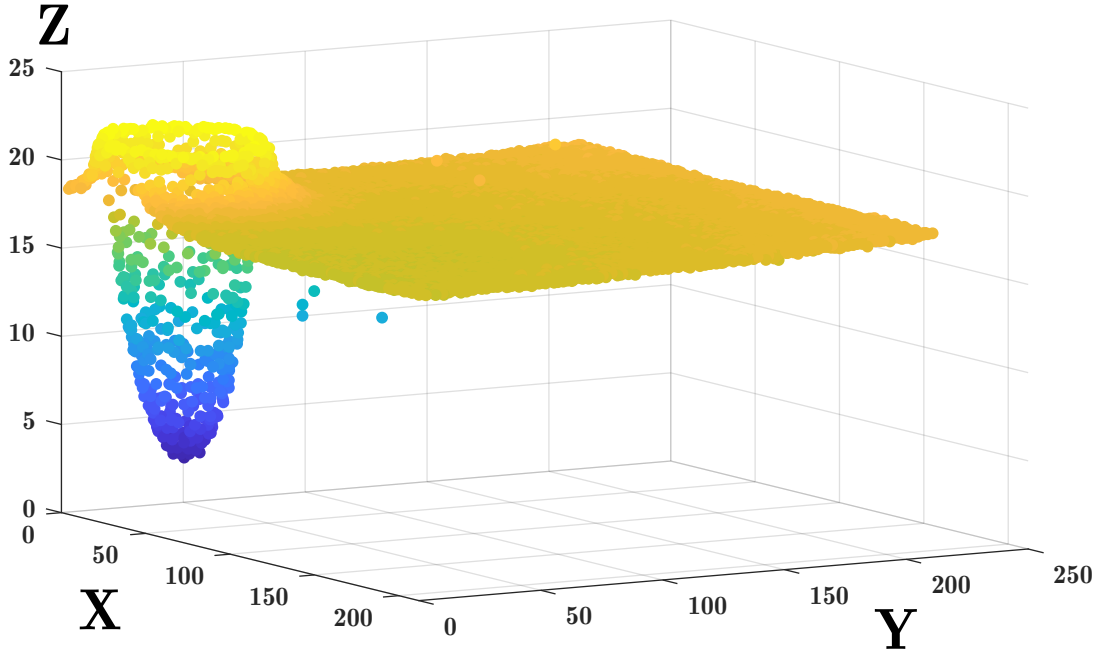


Figure 3.7: Fluorescent bead location for the same sphere as Fig. 3.6 with the vertical axis stretched to showcase the bead density under the bottom of the sphere. The colors just distinguish the depth of the fluorescent beads.

better indicate the resolution to which we try to fit a circle. Note the abrupt cut off around  $r = 26 \mu\text{m}$  and how the substrate is lifted up above the zero-plane due to adhesion. Also notice the flatness on of the substrate between  $r = 26\text{--}29 \mu\text{m}$ . Not all samples have this flat ridge; many spheres lift the substrate to a point which the immediately slopes downward back to the zero-plane. This behavior depends slightly on the sphere size, but it is mainly a reflection of the amount of phase-separation induced. This is a property of each silicone which depends on the environmental conditions.

It is important to be careful with the circle-fits in the case where the sphere is small enough to sink into the substrate with a depth  $d > r$ . In these instances, the side profile is non-continuous, and we only fit the sphere to the bottom portion of the profile before the break. An example of one of these sphere is shown in Figures 3.13 and 3.14.

After fitting the circle to the substrate's side profile, we can extract the depth vs. radius. The radius of the sphere equals the radius of the circle, and the depth is the lowest point of the circle in the z-plane, which we center at  $x = 0$  in Figures 3.11 and 3.12.

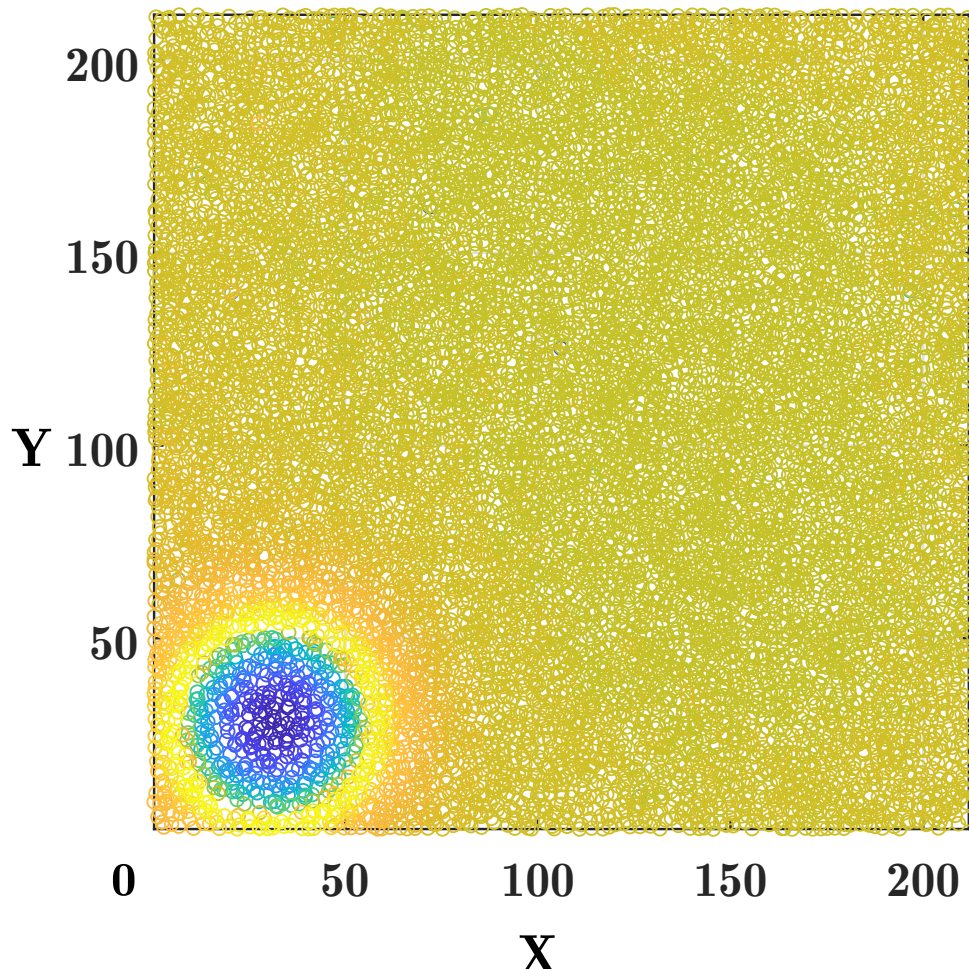


Figure 3.8: The top view of the same sphere as in the previous figures. This allows us locate the center of the bottom of the sphere. From this we can construct a side profile (Figure 3.9).

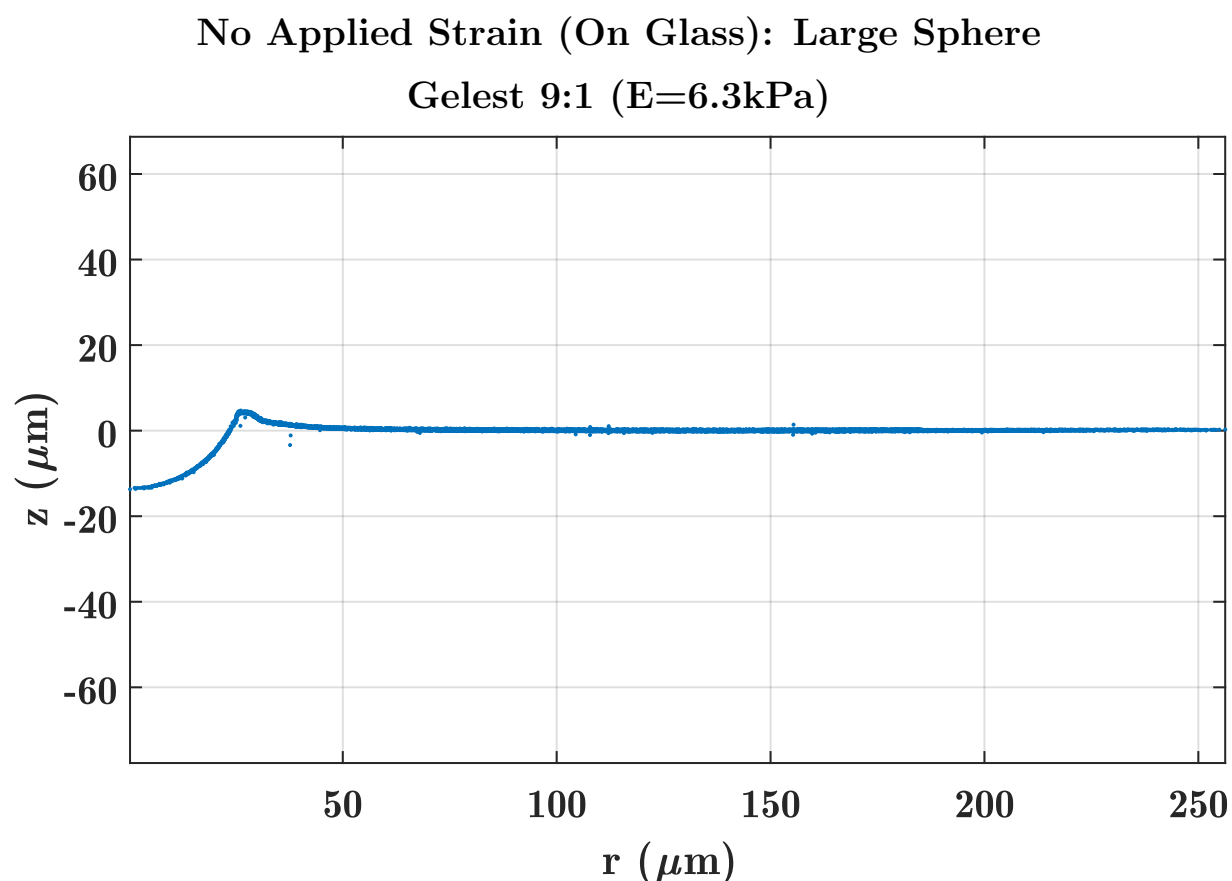


Figure 3.9: The full surface profile, collapsed azimuthally. From this, the region conforming to the adhered sphere is clearly visible

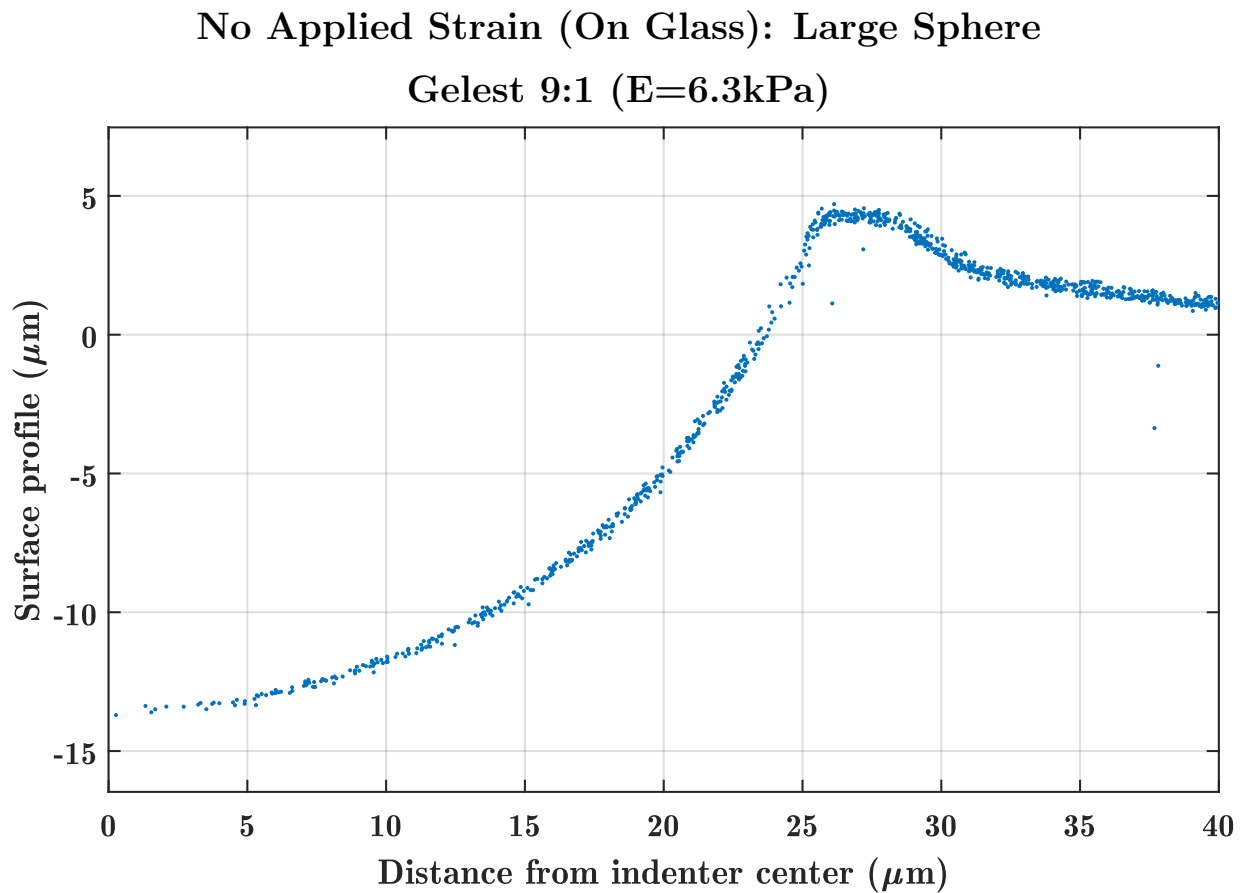


Figure 3.10: Zoomed-in version of Figure 3.9. It is useful to zoom in and see the the quality of the collapse. A dense collapse leads to a smaller margin of error in fitting a circle to the profile (See Fig. 3.11).

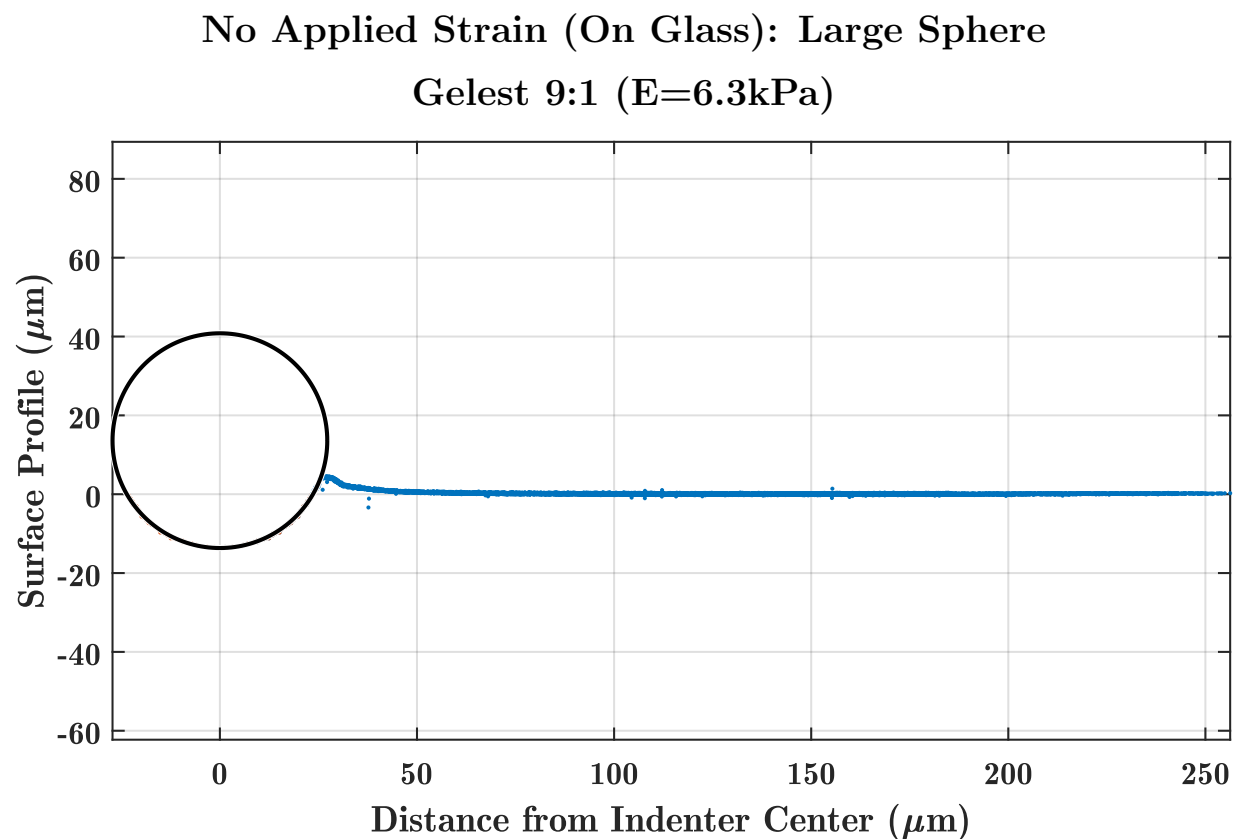


Figure 3.11: Same as in Figure 3.9, only with a circle fitted to the indentation sphere. Notice how the surface plane is completely flat and centered at a depth of 0.

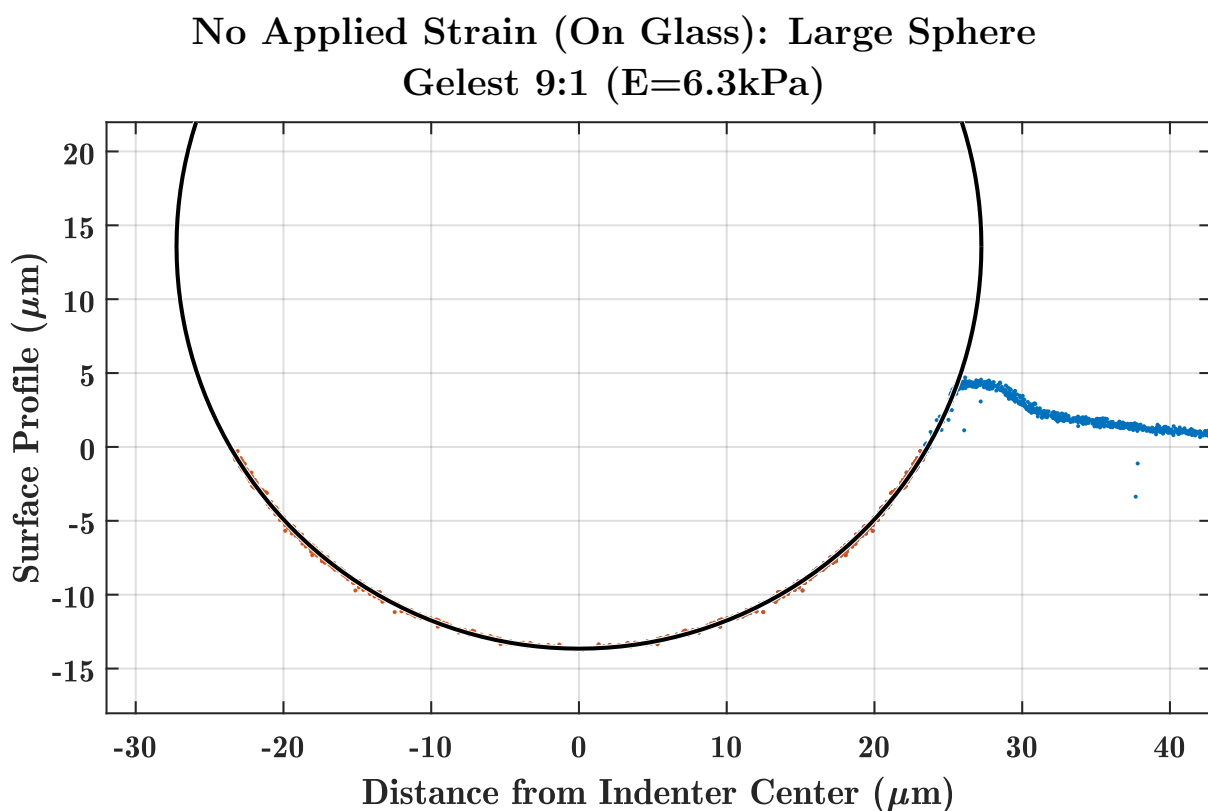


Figure 3.12: Zoomed in version of Figure 3.11. The orange dots are the data points being used to fit the circle. Note the sphere fits nicely in the indentation all the way up to the cusp, past the points being used for the fit.

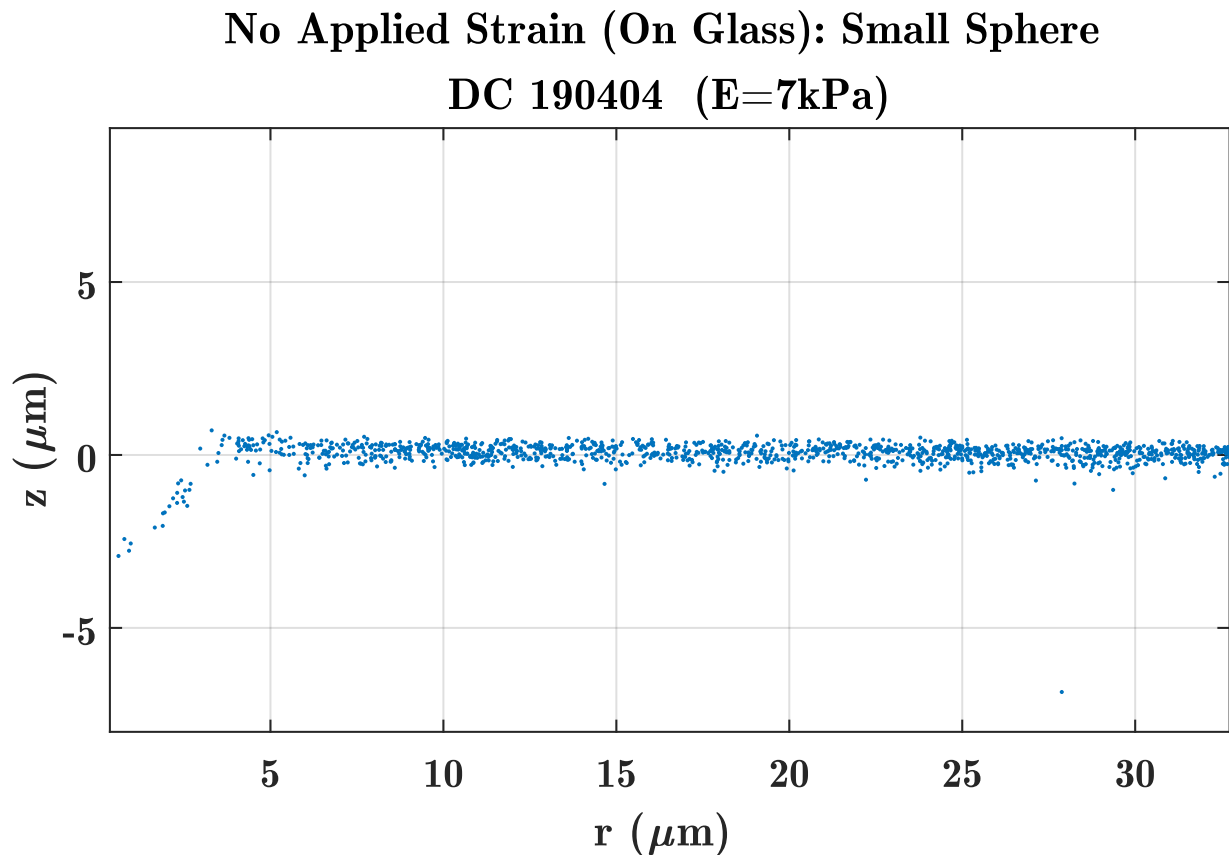


Figure 3.13: The collapsed side profile for small spheres has fewer fluorescent tracer particles to outline the sphere. There is often a break in the fluorescent bead coverage if the sphere sinks in deeper than its “waist.” In this example, the break in coverage just at  $-1 \mu\text{m}$ . This can be seen better in Figure 3.14 where the fluorescent beads from the bottom of the sphere up to the break are highlighted in orange.

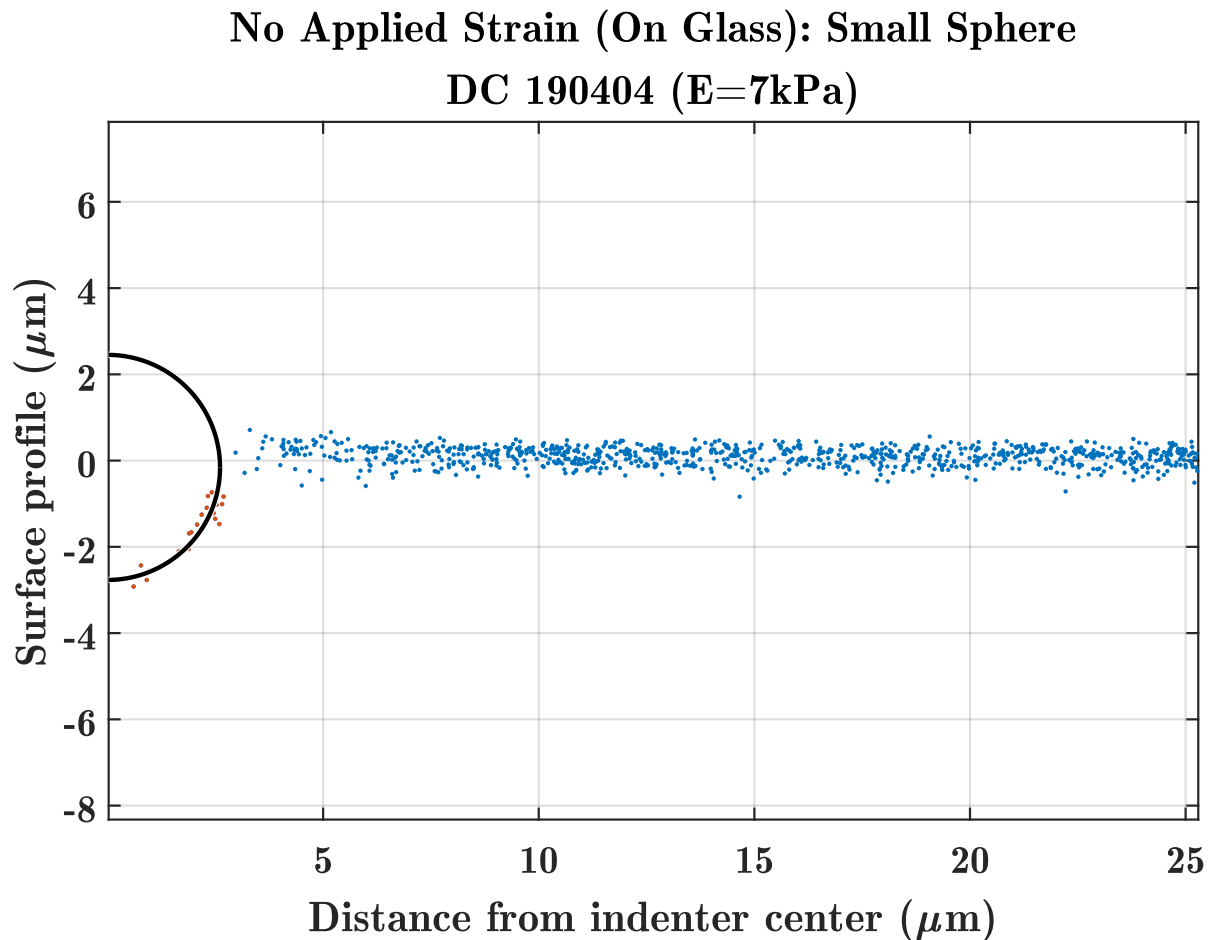


Figure 3.14: For a small sphere where  $r < d$ , there is generally a break in the sphere outline. For these circle-fits, only the fluorescent beads up to the break (colored in orange) are taken into account for the fit.

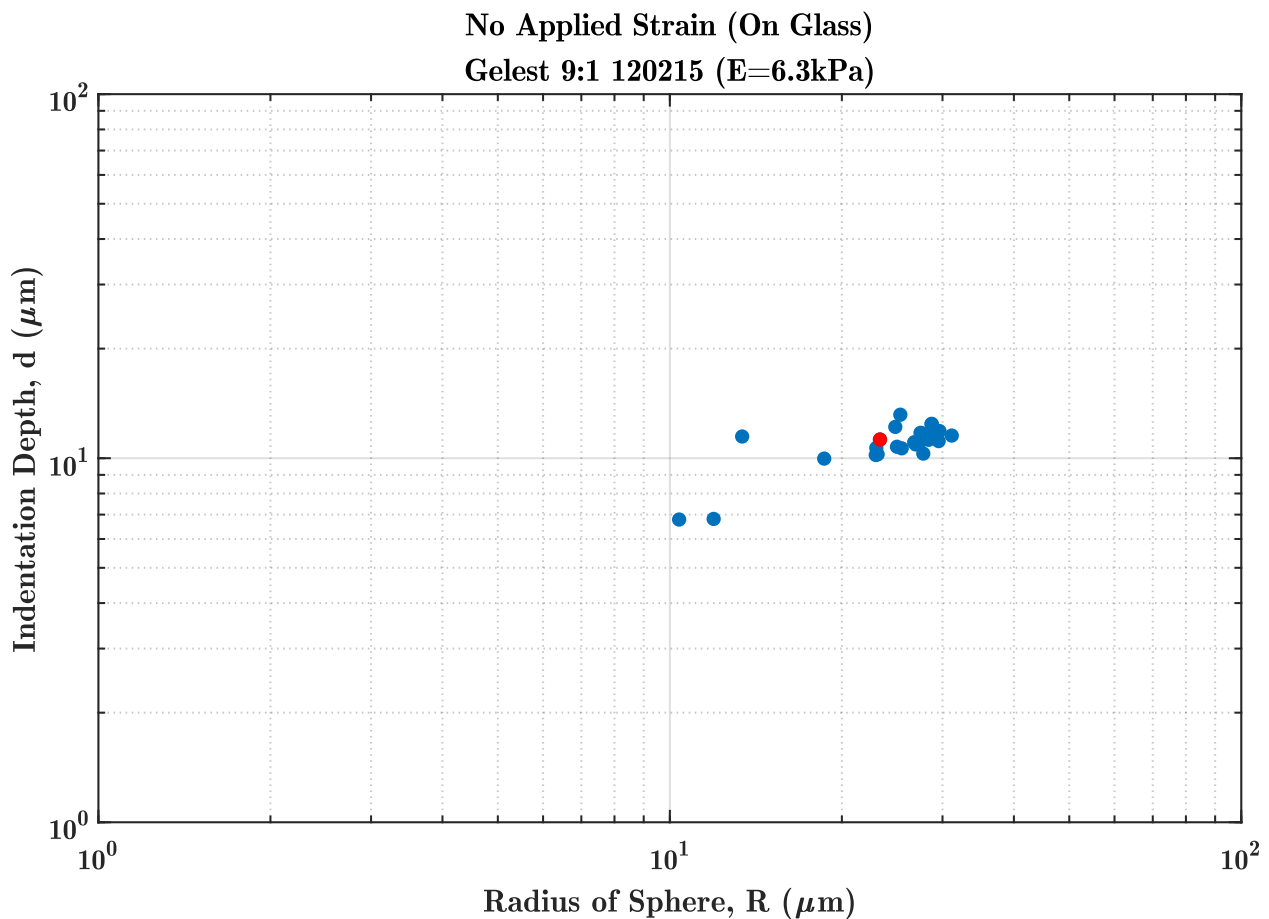


Figure 3.15: Plot of the spontaneous indentation depth vs. radius for a variety of silica spheres on a PDMS substrate. The red point indicates the same sphere that was examined in Figures 3.5 – 3.12.



# Chapter 4

## Surface Stress and Adhesion Results

In this chapter, we present preliminary surface stress and adhesion energy data collected for two types of silicone with various stiffnesses. We first used Gelest brand silicone to obtain our preliminary data and tune the operation of our device. We then switched to Dow-Corning brand silicone to continue more extensive measurements. First we give a brief background of the materials used.

### 4.1 Organosilicon Polymer Chemistry

PDMS, or Polydimethylsiloxane, is a commonly used polymer gel in the field of soft condensed matter. The gel is composed of a polymer network connected by crosslinkers, with additional free polymer in the fluid phase. When stretched, the large number of covalent bonds resist deformation on a macroscopic level.<sup>1</sup>

Below (Fig. 4.1) is the chemical structure for the vinyl-terminated PDMS (Gelest) that comprises the Gelest silicone. Dow-Corning is also a PDMS, but has an undisclosed molecular composition.

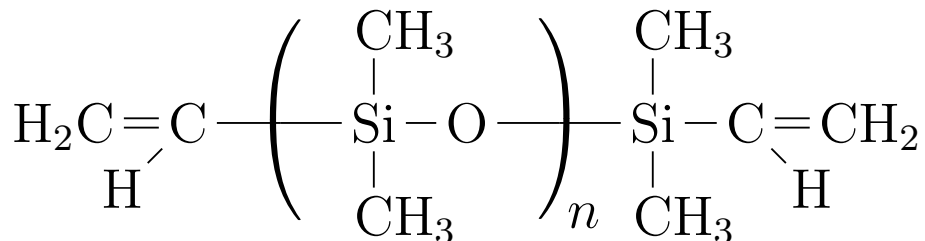


Figure 4.1: Divinyl-terminated Polydimethylsiloxane (DMS-V31)

<sup>1</sup>PDMS consists of covalent crosslinkers, however, many compliant materials are a result of physical crosslinkers (e.g. gelatin). When physical crosslinkers are stretched, the configuration of the system changes such that the tangled crosslinkers begin to unwind and untangle. From a statistical mechanics perspective, this decreases the configurational entropy, thus increasing the free energy [41].

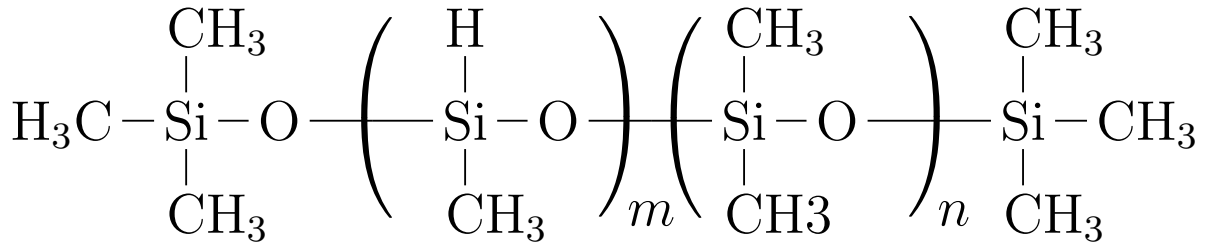


Figure 4.2: Trimethylsiloxane terminated 25–35% methylhydrosiloxane ( $m$ ) – dimethylsiloxane ( $n$ ). This is the crosslinker for Gelest silicone (HMS-301).

For Gelest, the crosslinker of the system is a trimethylsiloxane terminated 25–35% methylhydrosiloxane - dimethylsiloxane copolymer (Gelest HMS-301). The crosslinker is much shorter on average than the PDMS, containing roughly 20–30 repeating monomer groups. The single hydrogen on the methylhydrosiloxane is weakly bound and can be replaced by one of the hydrogen atoms in the PDMS. This bonding happens repeatedly, creating long twisted chains which comprise the mesh network of the gel. Increasing the density of crosslinkers provides an easy and controllable method to vary the gel’s stiffness [41].

Mix Ratio (A:B)	Young’s Modulus (kPa)	Sol Fraction (%)
7.5 : 1	2.5 ± 0.1	65.2
9 : 1	5.0 ± 0.1	64.7
11 : 1	10.0 ± 1	63.7

Table 4.1: PDMS gel characterization for Gelest silicone. By varying the relative density of the crosslinkers, one can predictably control the stiffness of the gel.

### 4.1.1 Silicone Preparation and Spin-Coating

Before spin-coating it is useful to coat the base with fluorescent beads to help determine the substrate’s thickness. The sole purpose of this coating is to help locate the substrate’s bottom surface, so a dense bead coverage is not required and could potentially be harmful if there is significant light bleeding<sup>2</sup>. To coat the base, we pipet 40 nm fluorescent beads onto the glass of PDMS and let sit for 30–60 seconds. Full directions for preparing a fluorescent bead solution can be found in Appendix B. After this time, we return the fluorescent beads back to the solution for re-use. A significant number of beads will remain on the base, however. To remove some excess, we gently wash the substrate with de-ionized water. For a glass coverslip, we simply submerge the entire slip in water and gently remove it at a

<sup>2</sup>When the light from the fluorophores is intense enough, they are detected in the adjacent images in the vertical stack. This phenomenon is referred to as “light bleeding.”

45° angle, using surface tension to prevent the water from breaking up into smaller droplets. This process is slightly more difficult for the petri dish due to the larger size. We have had success using 1000 mL beaker tilted at an angle, though any container with a large enough opening may substitute. It is also possible to use an autopipet for washing by simply repeating the same process used for the fluorescent bead coating, only with water instead this time. We have had mixed success with this technique, however; it leaves a water droplet on the surface and often creates an uneven coating of fluorescent beads, manifested as fluorescent streaks across the surface.

After the first layer of fluorescent beads is coated, it is time to spin-coat the soft substrate. We aim to make our spin-coated substrates around 80–100  $\mu\text{m}$  thick. Depending on the silicone, we wait a different amount of time before spin-coating onto the prepared base. This allows the curing process to increase the silicone's viscosity enough to remain on the base when spun. As an extreme example, consider trying to spin-coat water; it would all fling off the base. We coat our substrate onto coverslips for “zero applied strain” data or on PDMS sheets from SMI (Shore Durometer: 40, Thickness: 0.005”) for stretching data. Gelest 9:1 cures rapidly at room temperature, so no waiting time necessary. For Dow Corning 1:1, we wait 45–60 minutes after combining parts A and B before spin-coating.

To help with the evenness of the coating, we degas the gel by leaving it in a vacuum chamber for a few minutes. A few small bubbles are not of concern, as the process of transferring the gel to the base is enough to pop any remaining stragglers. We have found that a “glob” of gel roughly half the diameter of the base spin-coated at 500 rpm for 40 seconds is enough to create an even coating of roughly 100  $\mu\text{m}$  for both Gelest 9:1 and Dow-Corning 1:1 PDMS.

Coating a coverslip with silicone is a straightforward process where hardly anything can go wrong. Coating the stretchable PDMS base, however, requires some creativity to find the steps necessary to return the best results. We cut the SMI PDMS sheet with an X-acto knife and use a standard Petri dish (3.5” diameter) as a template. In order to avoid snagging, we cut out the disk before removing the paper sheets on both sides of the silicone and tape the Petri dish to the paper to help prevent the dish from slipping while cutting. Unlike the glass coverslip, the PDMS base is not rigid and must be placed on a firm surface, such as a Petri dish, for spin coating. This leaves the possibility for air bubbles to become trapped in between the PDMS and Petri dish interface, a surefire way to produce an unevenly coated substrate. To avoid this, we remove the top paper sheet from the newly cut PDMS, then place the Petri dish on the exposed silicone. This creates a Petri dish with a silicone disk on top and a paper sheet on top of that. We then remove the air bubbles by pressing on the silicone sheet from the center outwards. Finally, any tiny, remaining air bubbles can hopefully be removed by placing the Petri dish in a vacuum chamber for a few minutes. It is at this point that we coat the PDMS with fluorescent beads and wash (as described early) before placing the petri dish onto the spin-coater and proceeding as described above.

After spin-coating, the silicone requires time to cure. We cure Dow-Corning 1:1 at room temperature for at least 24 hours. For Gelest 9:1, we oven cure at 70° C for at least 24 hours. Either silicone can be cured at room temperature or in the oven so long as a sufficient amount

of time is waited, however, we have used these curing parameters to maintain consistency and parallel the techniques used in previous literature [1].

After the silicone cures, we coat the surface with fluorescent beads again. For the 40 nm bead solution prescribed in Appendix B, we allow the solution to soak for up to 1.5 minutes before removing and washing the substrate. While the fluorescent beads chosen are most susceptible to light at 440 nm, there is still the risk of photo-bleaching<sup>3</sup> the fluorophores, and it is worth dimming the lab lights when working with them.

## 4.2 Preliminary Data: Gelest

Because the 2017 measurement [1] (See Figure 1) was obtained using Dow-Corning PDMS, our intention from the start was to use this material in our adhesion based measurements. However, due to technical difficulties<sup>4</sup> we decided to use Gelest instead while we calibrated the process. In this chapter, we present these preliminary data because it shows that the surface stress for the substrate is increasing with strain.

### 4.2.1 Standard Candles

Not only do we measure the depth and radii for a range of spheres, but we also measure a select few spheres at every strain. This allows us to track how any given sphere is changing—increasing our confidence that the shift in  $\Upsilon$  and  $W$  is not just an artifact of noise—as well as provide a more palpable piece of evidence than just a comparison of averages. Below (Fig. 4.3) is the side profile for Gelest 9:1 ( $E = 6.3 \text{ kPa}$ ). Notice how the indentation profile shifts upwards (less deep) to be flattened when the substrate is stretched. This shift is expected if the surface stress is increasing (see equation 2.9).

The  $d$  vs.  $R$  data collected with substrates on our stretching apparatus have a lot of noise. As seen in Figure 4.5, the  $d$  vs.  $R$  data collected on glass is far cleaner than that collected on the stretcher when strained. We can see the trend that under strain, the spheres sink into the substrate less deeply. At 22% strain, we expect zero strain-stiffening of our elastic substrate, and conclude that this change in depth is a result of an increase of surface stress,  $\Upsilon$ . Unfortunately, the  $d$  vs.  $R$  values are too noisy/scattered to make a reasonable fit to extract  $W$  and  $\Upsilon$  values.

The collapsed side profiles for spheres on a stretched substrate (see Figures 4.3 and 4.4) do not “collapse” as cleanly as those for spheres on glass; one glass, the spread in fluorescent beads is narrower than for stretchable substrates. Furthermore, the side profiles are often tilted away from the surface profile, and require manual editing to correct the far field height. It is much more difficult, however, to adjust the tilt. This is further discussed in Section 4.4, and can be seen in Figure 4.9.

---

<sup>3</sup>When too much light is exposed to the fluorophores, a photochemical alteration causes them to no longer be able to fluoresce.

<sup>4</sup>The Dow-Corning silicone was back-ordered.

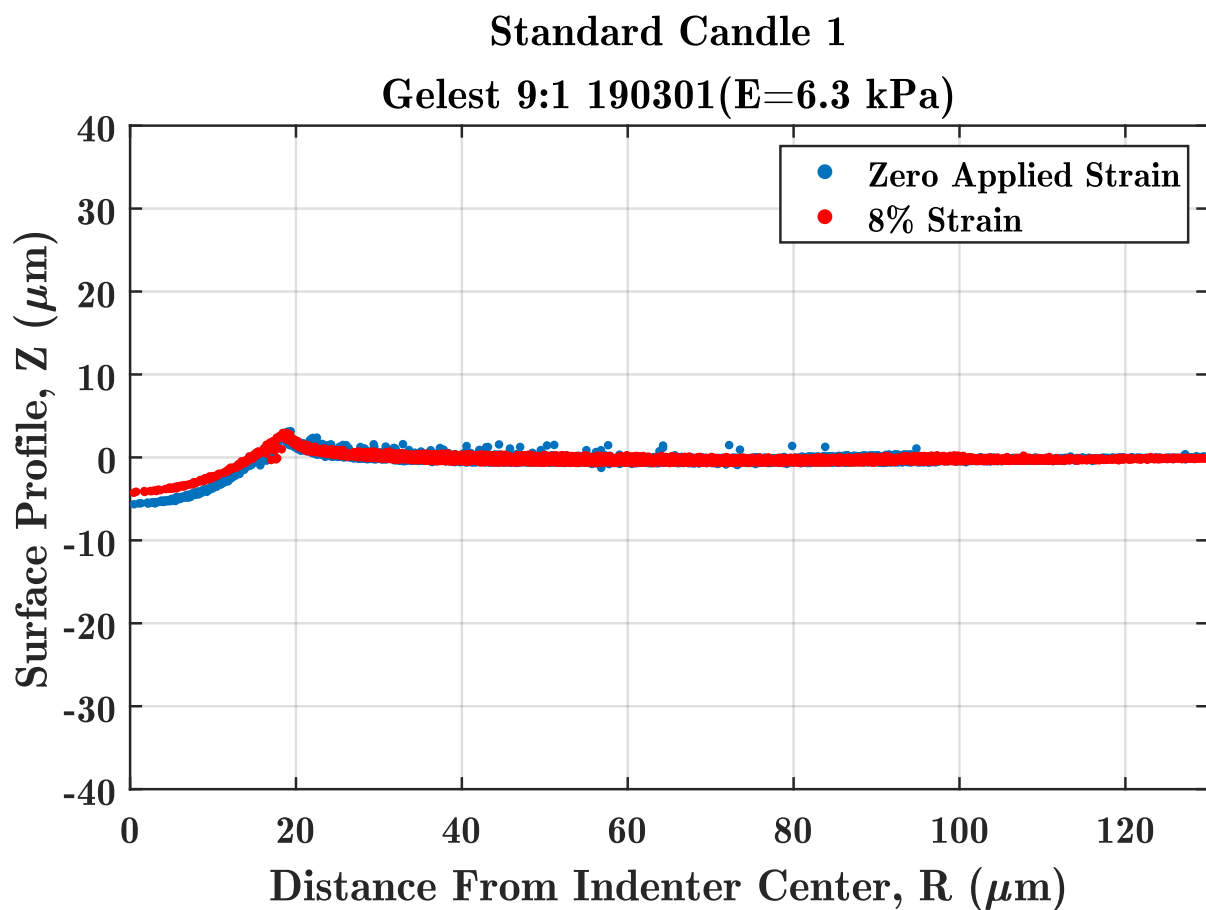


Figure 4.3: The side profile of the same sphere before and after stretch. Notice how after stretching, the sphere's indentation into the substrate is shallower.

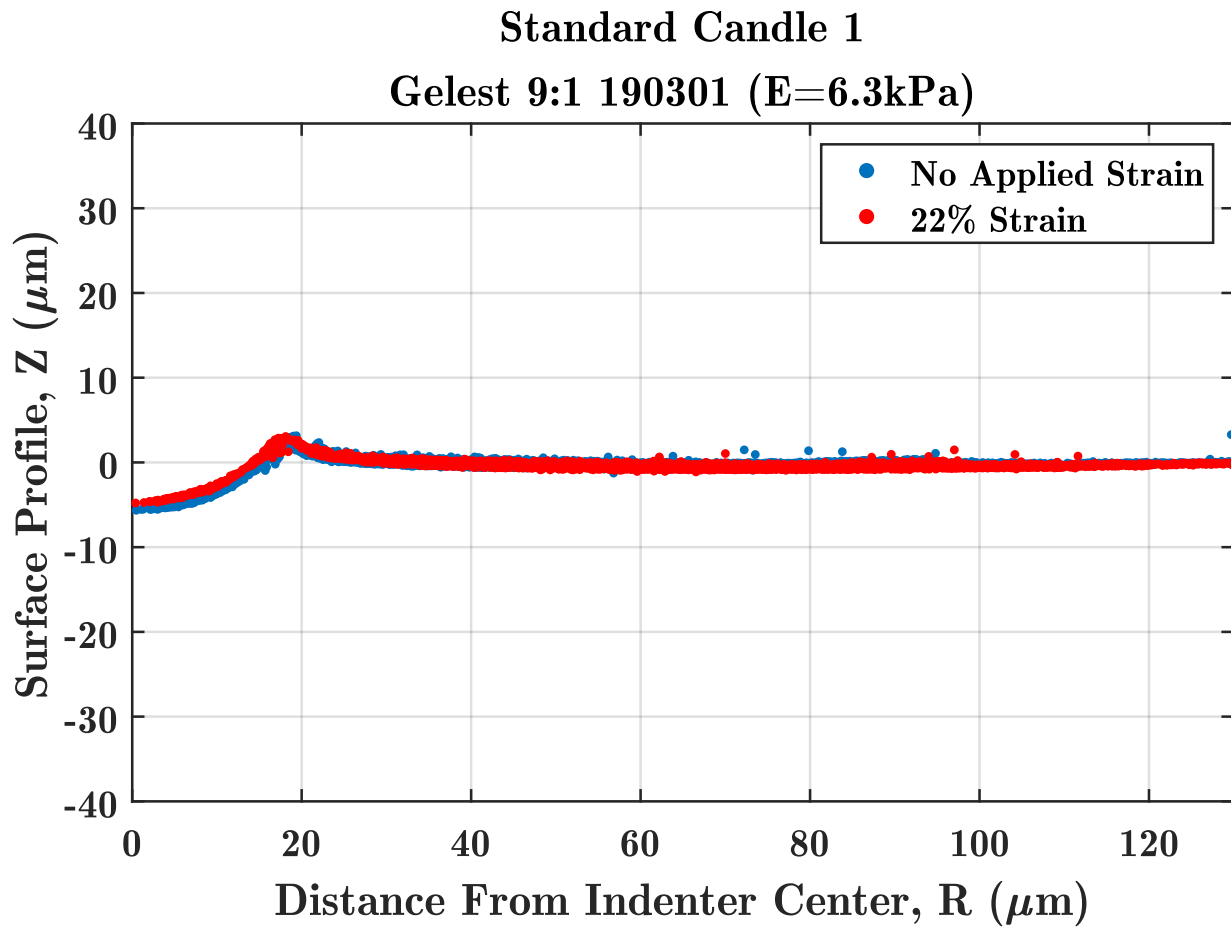


Figure 4.4: The side profile of the same sphere as in Figure 4.3 before and after stretch at 22% strain. Notice how after stretching, the sphere's indentation into the substrate is shallower.

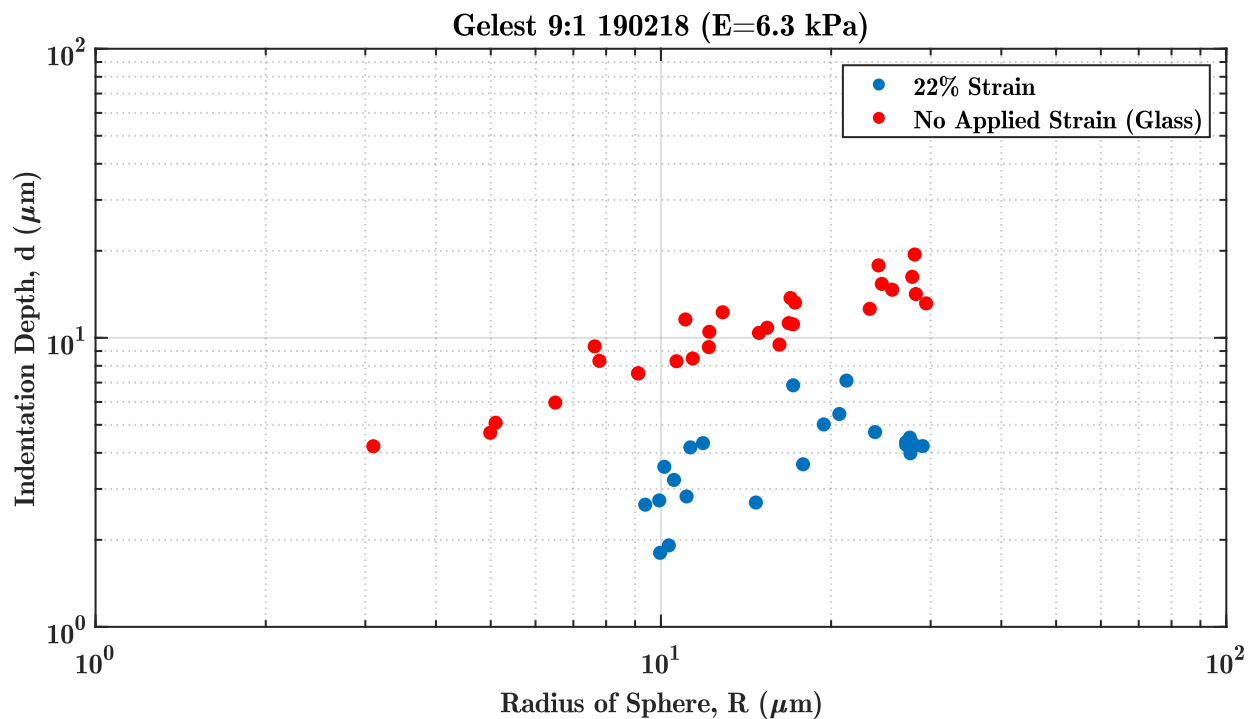


Figure 4.5: For Gelest 9:1, the silicone under strain (blue) on average sinks less deep into the silicone than for the same silicone sample spun on glass (zero applied strain). The large noise for the strain-data means we can not meaningfully determine  $\Upsilon$  and  $W$  to measure the variation in  $\Upsilon(\epsilon)$  and  $W(\epsilon)$ .

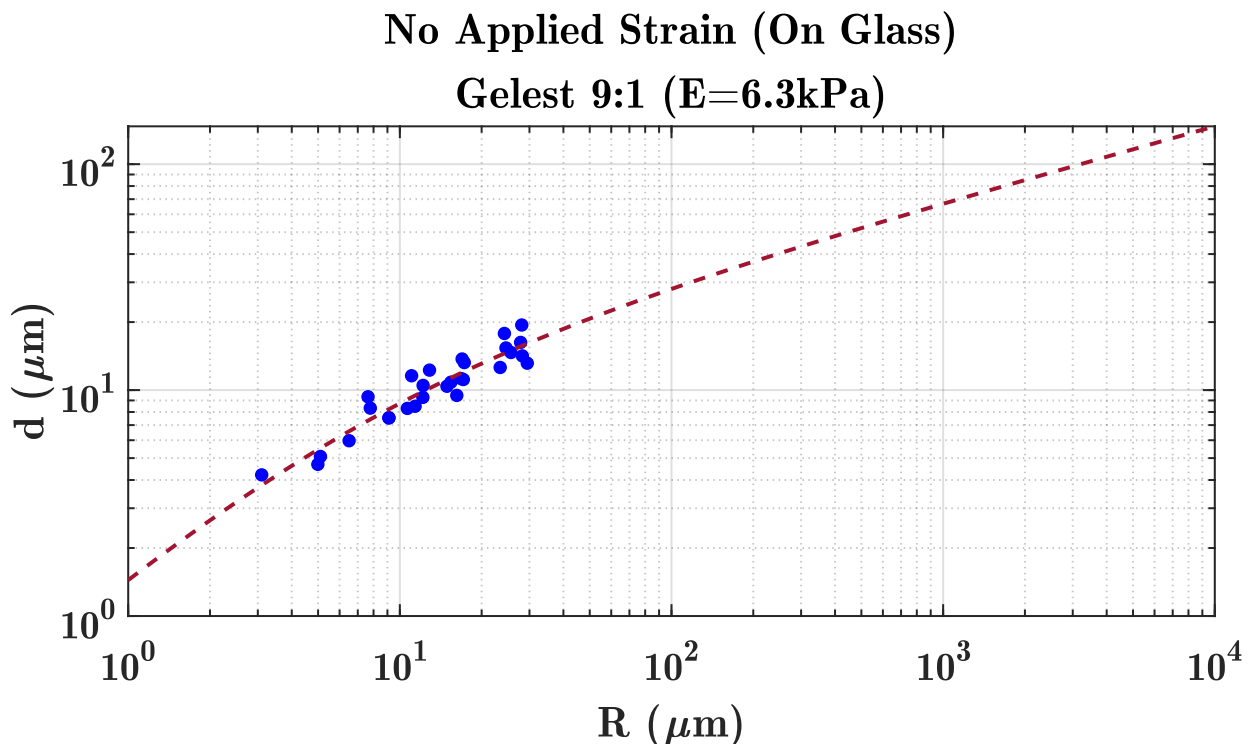


Figure 4.6: We fit Equation 2.9 to the  $d$  vs.  $R$  (depth vs. radius) plot for a Gelest 9:1 sample spun on glass. This is the same silicone sample as used in Figures 4.3–4.5. The best fit line returns parameters of  $W = 53 \text{ mNm}^{-1}$  and  $\Upsilon = 32 \text{ mNm}^{-1}$ . These values agree well with previous measurements (see Table 1.1).

### 4.3 Dow-Corning PDMS

Because the first direct  $\Upsilon(\epsilon)$  measurement [1] was conducted using a Dow-Corning PDMS substrate, we are especially interested in using this material for our first  $\Upsilon(\epsilon)$  measurements. Since there has only been one measurement of  $\Upsilon(\epsilon)$  in soft matter, in order to have a value to use as comparison, we need to first use the same material.

Our first measurements with Dow-Corning PDMS returned largely varying results; the stiffness of the silicone differed by a factor of 2 from the expected value, and the stiffness continued to increase as the silicone cured over a period of several weeks, as opposed to the usual 24 hour time-frame. Furthermore, the adhesion of the PDMS varied from sample to sample. Often the silica spheres would not adhere to the surface. It was eventually discovered that the Dow-Corning PDMS being used expired several years prior. Some of the measurements conducted, however, returned results of interest, and thus are included here.

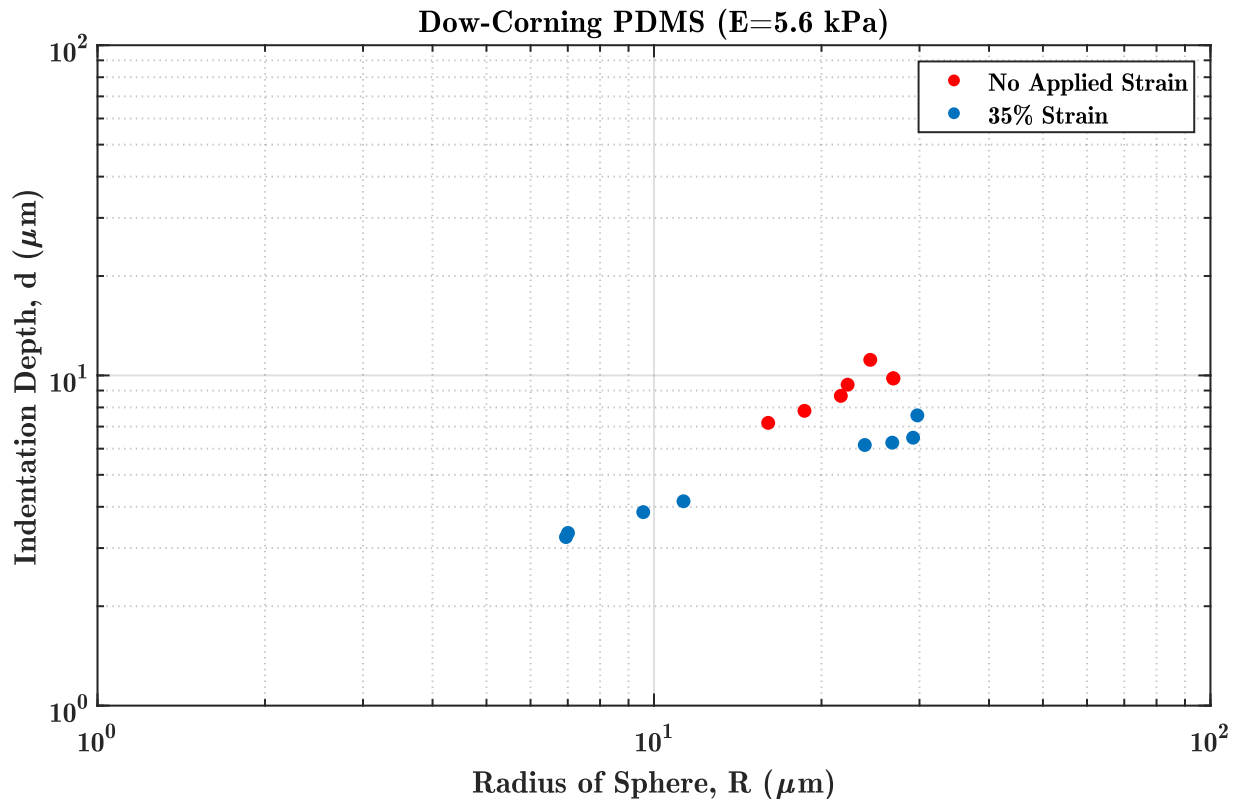


Figure 4.7: Plot of  $d$  vs.  $R$  for a Dow-Corning [expired] PDMS substrate (191118) at two different strains. At higher strain, the spheres sink in less deep. This can be explained by an increase in  $\Upsilon$  or an increase in  $E$  for the substrate.

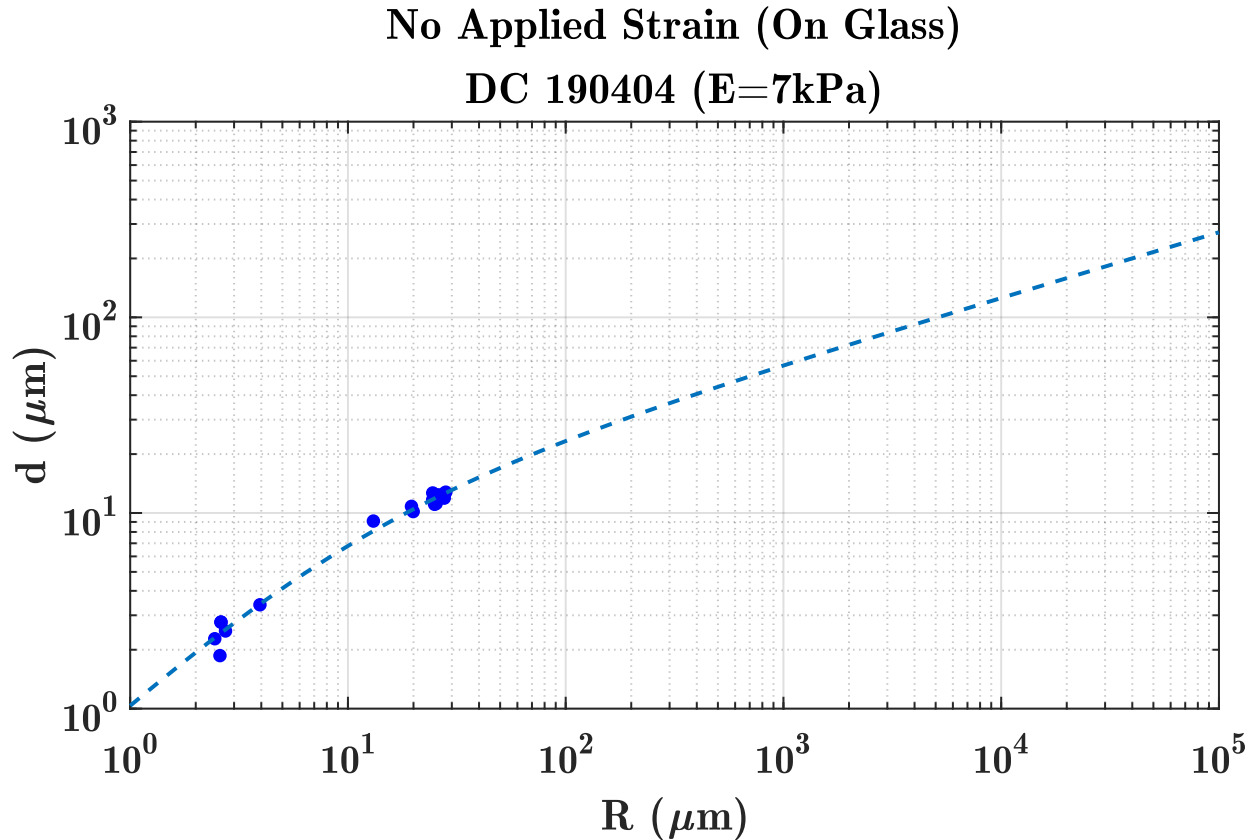


Figure 4.8: The surface stress and adhesion energy fit for new Dow Corning PDMS silicone with no applied strain. Given the  $d$  vs.  $R$  values, the fitting parameters to make the best fit line are  $W = 48.6 \text{ mNm}^{-1}$  and  $\Upsilon = 43.5 \text{ mNm}^{-1}$ .

#### 4.4 Gelest and Dow-Corning PDMS Conclusions

Our  $d$  vs.  $R$  data with the Gelest PDMS is clean for samples spun onto glass and returns reasonable values for  $\Upsilon$  and  $W$ . Furthermore, we see a clear change in indentation depth for the individually tracked spheres (standard candles) under strain (Figure 4.3). Additionally, the average indentation depth for the strained sample compared to that spun onto glass is significantly shallower (Figure 4.5). However, the  $d$  vs.  $R$  data collected for Gelest on the stretching apparatus is noisy. As a consequence, we have yet to extract  $\Upsilon(\epsilon)$  and  $W(\epsilon)$ . For Dow-Corning PDMS, our  $d$  vs.  $R$  data with the new material is clean for samples spun onto glass, and returns reasonable values for  $\Upsilon$  and  $W$ . As of the time writing, we have yet to test a stretchable sample of the new Dow-Corning PDMS.

Currently, the persistence of noise on our all  $d$  vs.  $R$  data collected on the stretching apparatus is the main factor constraining our  $\Upsilon(\epsilon)$  and  $W(\epsilon)$  measurements. We hypothesize that the noise stems a large tilt found in all the data collected for substrates on the stretching apparatus. Upon close scrutiny of the azimuthally collapsed surface profile (e.g. Figure 3.9)

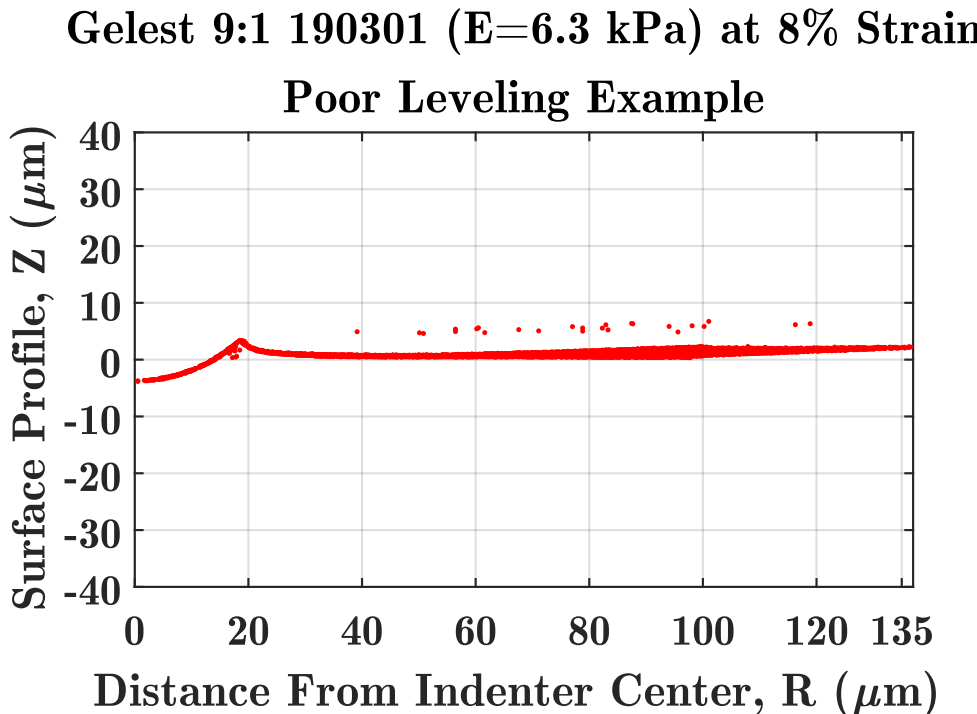


Figure 4.9: The side profile of a sphere on a stretched substrate. Notice how far away from the sphere, say  $R \approx 135$ , the surface is not at  $Z = 0$ , but instead a few microns above. For small tilts, such as those on a glass substrate, we can easily correct re-level the surface plane in using MATLAB software. However, the large tilts for the spheres collected on the stretching apparatus are problematic and not always correctable with software.

for spheres on stretchable substrates, many do not correctly “zero” the surface plane of the substrate. The surface profile is pulled up by the sphere due to adhesion, but returns to the surface plane far away from the sphere. However, for many of the spheres inspected, collapsing the side profile of the sphere caused the surface profile to be tilted away from zero far away from the sphere (See Figure 4.9). Conversely, leveling the profile has an adverse effect on the quality of the side collapse for the sphere. This tilt tends to be great enough such that the surface is between  $\pm 5 \mu\text{m}$  at a distance of  $140 \mu\text{m}$  from the sphere. While this is only a tilt of  $0.036^\circ$ , it means that the depth measurements are off by  $5 \mu\text{m}$ , a significant discrepancy that would account for the noise.

Our MATLAB software attempts to correct for small tilts by leveling the surface plane of the located fluorescent beads, however, we suspect that this tilt may be too large to account for using our current software. Instead we have attempted to physically remove the tilt by leveling the stretching apparatus’ mount. As of the date of writing, we have successfully leveled the mount, but have yet to collect data with this correction.



# Chapter 5

## Future Work

### 5.1 Noise Minimization

As covered in the previous chapter, the limiting factor for our  $\Upsilon(\epsilon)$  and  $W(\epsilon)$  measurements is the noise present for all  $d$  vs.  $R$  data collected on stretchable substrates. We believe this noise is a result of the uneven mount that holds the stretching apparatus on the microscope's stage. We have corrected the mount's tilt by sanding and re-gluing the sides of the mount; however, if this does not correct the tilt, there are still options to consider.

If the mount is still too uneven, we could put tiny piezoelectric step motors on three corners of the mount, allowing for precise leveling of the surface plane for each sphere during data collection. We believe this will not be necessary, however, and suspect the reduced tilt from its current state will be sufficient to level the surface plane in post via software.

Alternatively, we have been measuring the radius of the spheres by fitting a circle to the azimuthal collapse, or side profile (see Figure 3.12). Instead, we could fit a sphere to the three-dimensional indentation (such as Figure 3.6). The advantage of fitting a sphere rather than a circle would be the increased number of points used for the fitting. We do not suspect the circle-fitting used for measuring  $R$  has been contributing to the noise observed. However, this spherical fitting technique may be useful in measuring  $r$  for very small spheres, which have been problematic for the circle fits.

### 5.2 New Materials

The adhesion based technique for measuring  $\Upsilon(\epsilon)$  should be applicable to virtually any soft solid capable of being stretched. Naturally, we would like to expand our measurements beyond silicone. Hydrogels, aerogels, gelatins, and commercial adhesives, to name a few, are materials of interest.

In the lab, we have begun to explore hydrogels specifically, and have successfully spin-coated fluorescently marked glycerol-based gelatin gels onto glass coverslips appropriate for confocal microscopy.

We are also pursuing measurements with commercially-manufactured hydrogels, namely Swiss Gummy Bears. Measuring the strain dependent surface stress of a gummy bear presents challenges not present in PDMS silicone. For example, gummy bears come in a predefined size and shape. In order to spin coat them on our apparatus, we must first melt down the gummies. Gummy bears are composed primarily of gelatin and a glucose syrup.<sup>1</sup>

### 5.3 Future Techniques

Currently, we use equation 2.9 to run a two parameter fit for the surface stress,  $\Upsilon$ , and the adhesion energy,  $W$ . Alternatively, it is possible to measure the adhesion energy separately. This technique, though not critically important to the experiment, is worth exploring. Measuring  $W$  separately and comparing the measured value to the calculated value via the two parameter fit would inform us about the accuracy of our fit for the zero-strain data, and possibly the strain-data if the adhesion energy per area is independent of strain, i.e.  $W = W(\epsilon)$ .

---

<sup>1</sup>Unlike Gummibärli, American gummy bears use corn syrup. We expect the landscape of gummy candies to provide a rich array of materials for future experiments.

# Appendix A

## Stretching Apparatus Engineering Design Documents

### A.1 Details of Stretcher Design

Aluminum was chosen as the base material because of its sturdy yet malleable nature, making it an excellent material with which to mill. Acrylic was considered, but was not chosen because of its brittle nature; we were concerned about cracking when drilling the UNF threads connecting to the Luer-lock syringe.

The stretched sheet is laid over the lubricated apparatus and fixed in place using a 48.7mm diameter by 1.6mm thick rubber O-ring. A removable plastic ring is then placed on top of the o-ring and clamped down using a tension clamp attached to a fitted plastic base slotted for the stretching apparatus to sit. The plastic ring is constructed from an engineering plastic that came from a similar but malfunctioning device used by our colleagues at ETH Zürich. The outer ring could easily be laser cut from a plastic or milled out of aluminum if desired.

To pull a vacuum, a 1/4-28 UNF to female Luer connects the apparatus to a plastic 100ml Luer-lock syringe. We found a more consistent stretch was held by lining the inner walls of the syringe in more Dow Corning vacuum grease. The UNF to female Luer connector is stainless steel, and coated with Dow Corning vacuum grease. The inclusion of a small o-ring between the UNF threads and the cylindrical base proved critical in holding vacuum for sustained periods of time.

The vacuum pull was controlled by a Harvard Apparatus Elite 11 Syringe Pump. This allows us to have a consistent withdraw rate and control over the amount of air withdrawn down to the pico-liter level, a far greater precision than needed. Stretching was found to work best at maximum withdrawal rate. Our stretching apparatus has sustained a constant equibiaxial stretch at 35% strain for as long as 5 hours. Maximum strain percentage and duration of maintained stretch is yet to be fully tested.

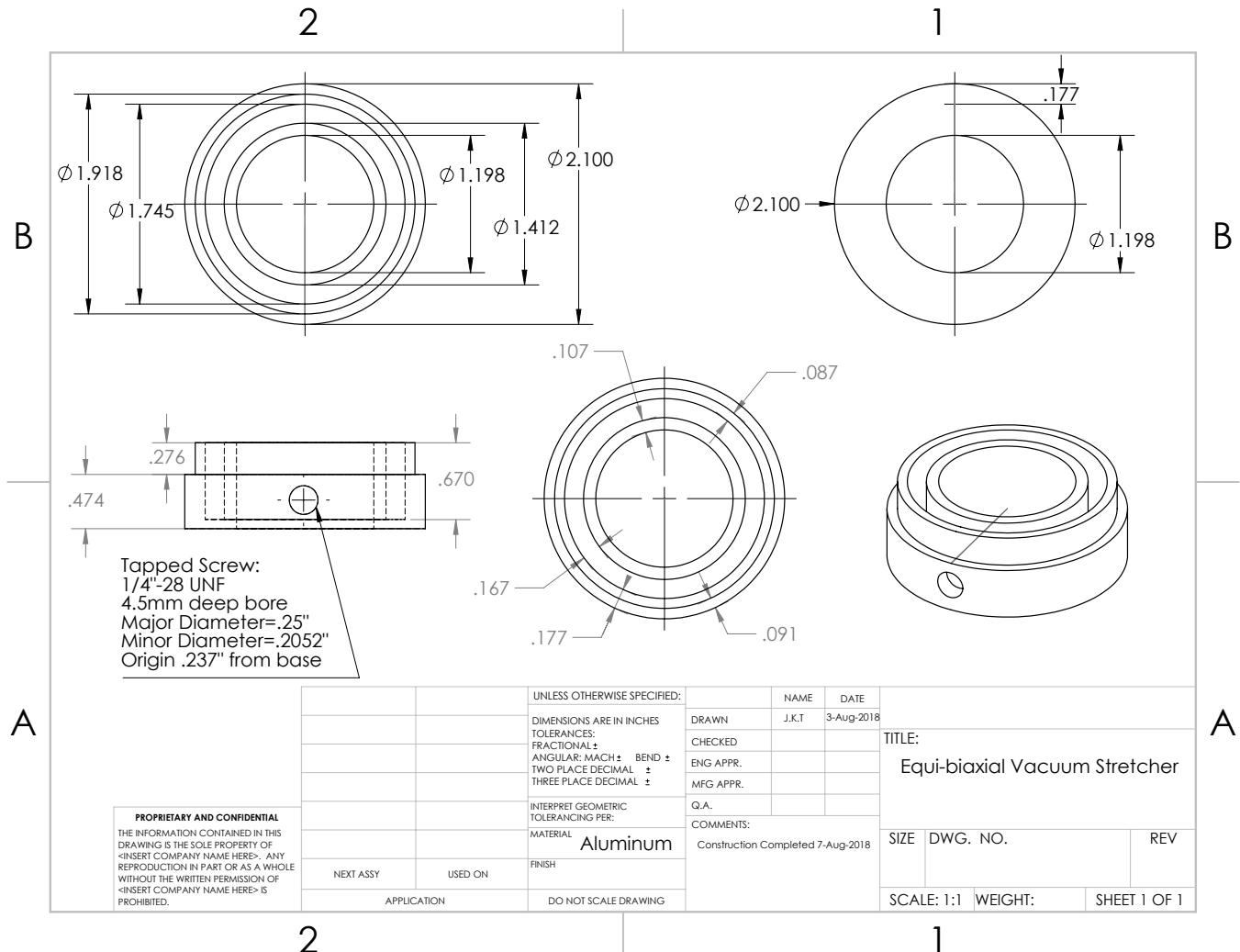


Figure A.1: The equi-biaxial vacuum stretcher design document. Note: all measurements are in inches.

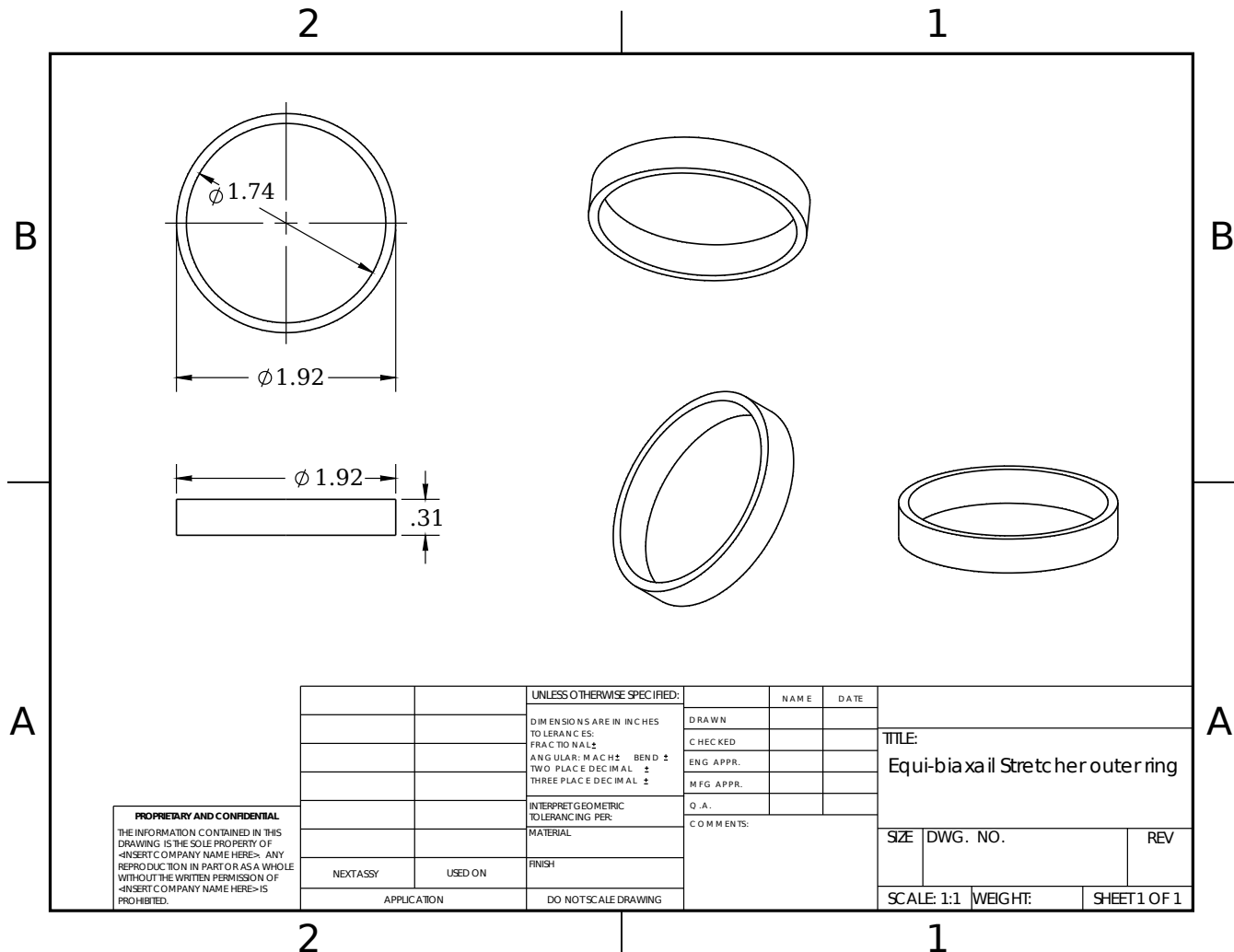


Figure A.2: Engineering Design Document of the outer-ring for the Stretching Apparatus.  
Note: all measurements are in millimeters.



# Appendix B

## Fluorescent Bead Recipe

### B.1 Preparation of a Fluorescent Bead Solution

To prepare the fluorescent bead solution, we first fill a 20 mL vial with a borate buffer solution. The instructions for preparing a bulk sample of this solution are placed at the end of this appendix. We then pipet 4  $\mu\text{L}$  of a concentrated fluorescent bead solution into the vial. We have been using 0.04  $\mu\text{m}$  yellow-green (505/515) carboxylate-modified FluoSpheres<sup>TM</sup> (5% solids) from Invitrogen<sup>TM</sup>. To minimize light exposure, we wrap the vial in tinfoil or colorful tape and store the vial in a refrigerator between uses. Before coating any substrate with the fluorescent bead solution, it is important to mix the solution thoroughly. We vortex the solution thoroughly before sonicating the vial for 5 minutes. This process helps to evenly distribute the fluorophores throughout the solution and minimize “clumping” for a more consistent coating.

#### Borate Buffer

- 400 mL de-ionized water
- 1.52 grams sodium tetraborate (Heat water to 70° and slowly add the sodium tetraborate to dissolve while stirring)
- 8.5 grams boric acid (add until pH is 7.4)



# Appendix C

## MATLAB Code

Below, we list and briefly explain the function of each MATLAB program used in analyzing the raw TIF images.

### C.0.1 Confocal Analysis Codes

Below I list the MATLAB codes used in analyzing the raw .ome.tif files obtained from the confocal imaging process. I will list them in the order executed to obtain the desired d vs. R values. In each description, I will also include the required files needed to run the script.

#### **`iterative_locating_input_parameters_2018.m`**

- Set particle locating parameters such as estimated particle size, brightness intensity range, and minimum separation
- Define the image stack to be analyzed
- Rescale the image from pixels to microns

#### **`iterative_particle_locating.m`**

- Locates the fluorescent beads
- Returns a .txt file with the locating information and creates a figure
- Produces Figure 3.6

#### **`process_and_collapse_confocal_data.m`**

- Estimate the center point of the sphere in the format of `[x,y] + return` using Figure 3.8
- Follow the directions printed on the screen to collapse the side profile of the sphere

- Produces Figure 3.9

#### **circle\_fit\_confocal\_profiles.m**

- You must edit this script for the first time you analyze a sphere for a given data set.
- This script fits a circle to the collapsed side profile
- Script saves the d vs r value as a .mat file, adds the [d,R] data to a list of all [d,R] values (or creates that list if it's the first time being run for a data set), and plots the d vs. R data
- Produces Figure 3.11

### **C.0.2 Strain Calculation Codes**

The codes used for calculating the strain are credited to Rob Style and Ross Boltyauski

#### **master\_tracking\_gui.m**

- This program requires many additional scripts, though it has easy to follow directions. Instead, we provide example code for measuring the strain. The final output is ‘C,’ the strain-tensor, and ‘T,’ the displacement vector.
- `params = master_tracking_gui('sample1_unstretched.tif')`
- `params(2) = master_tracking_gui('sample1_stretched.tif')`

#### **stretch\_est\_gui.m**

- Now grab the peak positions out of the data structure:
- `r = params(1).pks(:,1:2)`
- `r2 = params(2).pks(:,1:2)`
- `[A,t] = stretch_est(r,r2)`
- `[C,T] = stretch_refine(r,r2,A,t,2,1)`

### **C.0.3 Silicone Characterization Measurements**

To measure the stiffness of our silicone (Young Modulus, E), we use the TA XTPlus Texture Analyzer. We measure the force of resistance (N) vs. depth of compression (m) for several points near the center of the bulk, which we export as .txt files. We only use points near the center to isolate the silicone. Measuring near the sides could include the restorative force from the walls of the container.

**measure\_modulus.m**

- Calculates the average slope of this curve. This is the Young Modulus of the substrate. ( $\sigma/\epsilon$ )
- The requested starting position is the x-axis value where the linear slope approximately begins. It is better to overshoot the starting value than undershoot it



# References

- [1] Q. Xu, K. E. Jensen, R. Boltyanskiy, R. Sarfati, R. W. Style, and E. R. Dufresne. *Direct measurement of strain-dependent solid surface stress*. Nature Communications, 8(1):555 (2017).
- [2] P. de Gennes, D. Quere, and F. Brochard-Wyart. *Capillarity and wetting phenomena : drops, bubbles, pearls, waves*. Springer, New York (2003).
- [3] R. C. Cammarata and K. Sieradzki. *Surface and interface stresses*. Annual Review of Materials Science, 24(1):215–234 (1994).
- [4] J. W. Gibbs. *The scientific papers of J. Willard Gibbs*, volume 1. Longmans, Green and Company (1906).
- [5] M. E. Gurtin and A. I. Murdoch. *Surface stress in solids*. International Journal of Solids and Structures, 14(6):431 – 440 (1978).
- [6] C. Mays, J. Vermaak, and D. Kuhlmann-Wilsdorf. *On surface stress and surface tension: II. determination of the surface stress of gold*. Surface science, 12(2):134–140 (1968).
- [7] H. Wasserman and J. Vermaak. *On the determination of a lattice contraction in very small silver particles*. Surface Science, 22(1):164–172 (1970).
- [8] R. Hanneman, M. Finn, and H. Gatos. *Elastic strain energy associated with the “a” surfaces of the iii-v compounds*. Journal of Physics and Chemistry of Solids, 23(11):1553–1556 (1962).
- [9] R. E. Martinez, W. M. Augustyniak, and J. A. Golovchenko. *Direct measurement of crystal surface stress*. Physical Review Letters, 64(9):1035 (1990).
- [10] A. Schell-Sorokin and R. Tromp. *Mechanical stresses in (sub) monolayer epitaxial films*. Physical Review Letters, 64(9):1039 (1990).
- [11] R. E. Miller and V. B. Shenoy. *Size-dependent elastic properties of nanosized structural elements*. Nanotechnology, 11(3):139 (2000).

- [12] R. Dingreville, J. Qu, and M. Cherkaoui. *Surface free energy and its effect on the elastic behavior of nano-sized particles, wires and films*. Journal of the Mechanics and Physics of Solids, 53(8):1827–1854 (2005).
- [13] H. Duan, J. Wang, Z. Huang, and B. L. Karihaloo. *Eshelby formalism for nano-inhomogeneities*. Proceedings of the Royal Society A: Mathematical, Physical and Engineering Sciences, 461(2062):3335–3353 (2005).
- [14] P. Sharma and S. Ganti. *Size-dependent eshelby’s tensor for embedded nano-inclusions incorporating surface/interface energies*. Transactions-American Society of Mechanical Engineers Journal of Applied Mechanics, 71(5):663–671 (2004).
- [15] J. He and C. M. Lilley. *Surface effect on the elastic behavior of static bending nanowires*. Nano Letters, 8(7):1798–1802 (2008).
- [16] D. Lu, Y. M. Xie, Q. Li, X. Huang, and S. Zhou. *Towards ultra-stiff materials: surface effects on nanoporous materials*. Applied Physics Letters, 105(10):101903 (2014).
- [17] R. W. Style et al. *Stiffening solids with liquid inclusions*. Nature Physics, 11(1):82 (2015).
- [18] S. Mora and Y. Pomeau. *Softening of edges of solids by surface tension*. Journal of Physics: Condensed Matter, 27(19):194112 (2015).
- [19] S. Mora, T. Phou, J.-M. Fromental, L. M. Pismen, and Y. Pomeau. *Capillarity driven instability of a soft solid*. Physical Review Letters, 105(21):214301 (2010).
- [20] E. R. Jerison, Y. Xu, L. A. Wilen, and E. R. Dufresne. *Deformation of an elastic substrate by a three-phase contact line*. Physical Review Letters, 106(18):186103 (2011).
- [21] R. W. Style, R. Boltyanskiy, Y. Che, J. Wetlaufer, L. A. Wilen, and E. R. Dufresne. *Universal deformation of soft substrates near a contact line and the direct measurement of solid surface stresses*. Physical Review Letters, 110(6):066103 (2013).
- [22] Q. Xu, R. W. Style, and E. R. Dufresne. *Surface elastic constants of a soft solid*. Soft matter, 14(6):916–920 (2018).
- [23] H. Liang, Z. Cao, Z. Wang, and A. V. Dobrynin. *Surface stresses and a force balance at a contact line*. Langmuir, 34(25):7497–7502 (2018).
- [24] R. W. Style, C. Hyland, R. Boltyanskiy, J. S. Wetlaufer, and E. R. Dufresne. *Surface tension and contact with soft elastic solids*. Nature Communications, 4:2728 (2013).
- [25] Y. Tian, M. Ina, Z. Cao, S. S. Sheiko, and A. V. Dobrynin. *How to measure work of adhesion and surface tension of soft polymeric materials*. Macromolecules, 51(11):4059–4067 (2018).

- [26] Z. Cao, M. J. Stevens, and A. V. Dobrynin. *Elastocapillarity: Adhesion and wetting in soft polymeric systems*. Macromolecules., 47(18):6515–6521 (2014).
- [27] Z. Cao, M. J. Stevens, and A. V. Dobrynin. *Adhesion and wetting of nanoparticles on soft surfaces*. Macromolecules, 47(9):3203–3209 (2014).
- [28] X. Xu, A. Jagota, D. Paretkar, and C.-Y. Hui. *Surface tension measurement from the indentation of clamped thin films*. Soft Matter, 12(23):5121–5126 (2016).
- [29] K. E. Jensen et al. *Wetting and phase separation in soft adhesion*. Proceedings of the National Academy of Sciences, 112(47):14490–14494 (2015).
- [30] S. Mondal, M. Phukan, and A. Ghatak. *Estimation of solid–liquid interfacial tension using curved surface of a soft solid*. Proceedings of the National Academy of Sciences, 112(41):12563–12568 (2015).
- [31] A. Jagota, D. Paretkar, and A. Ghatak. *Surface-tension-induced flattening of a nearly plane elastic solid*. Physical Review E, 85(5):051602 (2012).
- [32] N. Nadermann, C.-Y. Hui, and A. Jagota. *Solid surface tension measured by a liquid drop under a solid film*. Proceedings of the National Academy of Sciences, 110(26):10541–10545 (2013).
- [33] S. J. Park, B. M. Weon, J. San Lee, J. Lee, J. Kim, and J. H. Je. *Visualization of asymmetric wetting ridges on soft solids with x-ray microscopy*. Nature Communications, 5:4369 (2014).
- [34] K. L. Johnson. *Contact mechanics*. Cambridge University Press, Cambridge (1985).
- [35] K. L. Johnson, K. Kendall, and A. Roberts. *Surface energy and the contact of elastic solids*. Proceedings of the Royal Society A, 324(1558):301–313 (1971).
- [36] H. R. Hertz. *Über die berührung fester elastischer korper*. Verhandlung des Vereins zur Beförderung des Gewerbeleises, Berlin, p. 449 (1882).
- [37] Z. Cao and A. V. Dobrynin. *Nanoparticles as adhesives for soft polymeric materials*. Macromolecules, 49(9):3586–3592 (2016).
- [38] S. Na, A. Trache, J. Trzeciakowski, Z. Sun, G. Meininger, and J. Humphrey. *Time-dependent changes in smooth muscle cell stiffness and focal adhesion area in response to cyclic equibiaxial stretch*. Annals of Biomedical Engineering, 36(3):369–380 (2008).
- [39] M. Minsky. *Microscopy Apparatus*. US Patent Number 3013467. (1961).
- [40] Nikon Corporation, 1300 Walt Whitman Road, Melville, N.Y. 11747-3064, U.S.A. *A1 HD25 A1R HD25 Brochure* (2018).
- [41] J. H. S. Bruno Andreotti. *Statics & dynamics of soft wetting*. Annual Review of Fluid Mechanics (2020).